

# RESEARCH ACTIVITIES IX

## Research Center for Molecular-Scale Nanoscience

### IX-A Nano-Science and Nano-Technology toward Molecular Scale Electronics

Molecular electronics is a fairly new and fascinating area of research that is firing the imagination of scientists. However, most single organic molecules are not conductive in a classical sense, long range electronic transport through single molecules can not be so effective to realize practical electronic circuits. Our group is interested in (1) construction of nano-structures made from conductive materials such as carbon nanotubes, metal particles or rods, with functional organic molecules, (2) measurements of electric or photonic properties of individual nano-structures while observing their nanometric images, and (3) conductance change of single molecules by external stimulation such as electric field, photon irradiation or chemical species.

#### IX-A-1 Photo Precursor for Pentacene

UNO, Hidemitsu<sup>1</sup>; YAMASHITA, Yuko<sup>2</sup>;  
KIKUCHI, Makoto<sup>2</sup>; WATANABE, Hikaru<sup>2</sup>;  
YAMADA, Hiroko<sup>2</sup>; OKUJIMA, Tetsuo<sup>2</sup>; OGAWA,  
Takuji<sup>3</sup>; ONO, Noboru<sup>2</sup>  
(<sup>1</sup>Ehime Univ., JST; <sup>2</sup>Ehime Univ.; <sup>3</sup>IMS, JST)

[*Tetrahedron Lett.* **46**, 1981–1983 (2005)]

Pentacene is one of the most sensational polycyclic hydrocarbons, which draws attention from many fields due to its high electron mobility. Many efforts have been focused on the device preparation of not only pentacene itself but also its derivatives. For the application of pentacene and its derivatives, one of the biggest problem is the low solubility in common solvents. Difficulties are often encountered in the purification of its derivatives, and several manipulations of a high vacuum sublimation are required. In the final stage of pentacene based devices, the vapor deposition technique under high vacuum is usually employed. In order to overcome the problem, precursors, which give pentacene or its derivatives by thermal decomposition, namely retro Diels-Alder reaction, were developed and their applications for field effect transistors (FET) and organic thin film transistors (OTFT) were recently reported. In these cases, retro Diels-Alder reaction of the precursors was designed to proceed at rather low temperatures by extrusion of tetrachlorobenzene and *N*-sulfinylacetamide. The requisite for such leaving molecules is sufficiently small and inert not to affect the property of pentacene devices. For these precursor methods, there is an inevitable drawback that the high vacuum sublimation technique, one of the most reliable and successful device preparation methods, cannot be applied, because the trigger of the precursors to pentacene is heat. We thought that not only this shortcoming of the precursor method but also property of the leaving molecules can be dramatically improved if the alternative physical decomposition method, namely light, is applied. In this communication, we report preparation of the first photo-convertible precursor to pentacene and its fundamental properties.

#### IX-A-2 Synthesis and Self-Assembly of Novel Porphyrin Molecular Wires

KAWAO, Masahiro<sup>1</sup>; OZAWA, Hiroaki<sup>2</sup>;  
TANAKA, Hirofumi<sup>3</sup>; OGAWA, Takuji<sup>3</sup>  
(<sup>1</sup>Ehime Univ., JST; <sup>2</sup>SOKENDAI, JST; <sup>4</sup>IMS, JST)

[*Thin Solid Films* in press (2005)]

Sub-micrometer long butadiyne-linked porphyrin wires were synthesized by oxidative coupling of diethynylporphyrin. The porphyrin wires were analyzed by analytical gel permeation chromatography, absorption spectroscopy and matrix-assisted laser desorption/ionization time of flight mass spectroscopy. Observations of the wire were performed by atomic force microscopy. Self-assembled structures of the wires were observed on highly oriented pyrolytic graphite. Self-assembling features of the porphyrin wires depended on the length of the porphyrin wires and the concentration of the depositing solution.

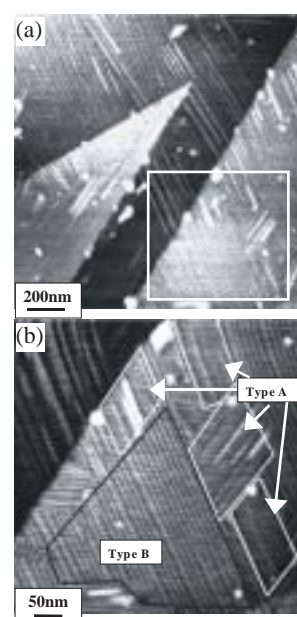


Figure 1.

### IX-A-3 Molecular Junctions Composed of Oligothiophene Dithiol Bridged Gold Nanoparticles Exhibiting Photoresponsive Properties

HUANG, Wei<sup>1</sup>; MASUDA, Gou<sup>2</sup>; MAEDA, Seisuke<sup>2</sup>; TANAKA, Hirofumi<sup>3</sup>; OGAWA, Takuji<sup>3</sup>  
(<sup>1</sup>Nanjing Univ.; <sup>2</sup>Ehime Univ.; <sup>3</sup>IMS, JST)

[Chem. Eur. J. 12, 607 (2006)]

Three oligothiophene dithiols with different number of thiophene rings (3, 6 or 9) were synthesized and characterized. X-ray single crystal structures of compounds 3',4'-dibutyl-5'5''-dithiocyanato-2,2':5',2''-terthiophene (**2**) and 5,5''''-dithiocyanato-tetrabutyl-2,2':5',2''':5'',2''':5''''-hexathiophene (**5**) were involved herein to show the exact molecular lengths as well as the difference between their UV-vis spectra arising from the different packing modes. These dithiols with different chain lengths were then treated with *t*-dodecanethiol protected active gold nano-particles (Au-NPs) *via* in situ thiol-to-thiol ligand exchange in the presence of 1 μm gap Au-electrodes. Thus the molecular junctions composed of self-assembled films were prepared, where oligothiophene dithiol bridged Au-NPs were attached to two electrodes by means of Au-S bonded contacts. The morphologies and *I-V* characteristics of these films were studied by SEM and AFM approaches, which suggest the thickness of the films varied within the size of one isolated Au-NPs and typical distance dependent semiconductor properties could be observed. Current-voltage (*I-V*) measurements for these devices were performed where the films served as active elements in the temperature range 6 ~ 300 K and classical Arrhenius plots and their linear fittings were carried out to give the activation energies ( $\Delta E$ ). Furthermore, preliminary studies on the photoresponsive properties of these junctions were explored at 80, 160 and 300 K, respectively. Physical and photochemical mechanisms were used to explain the possible processes. To the best of our knowledge, this is the first report where oligothiophene dithiols act as bridging units to link Au-NPs, and also the first report about functionalized Au-NPs exhibiting photo response properties in the solid state.

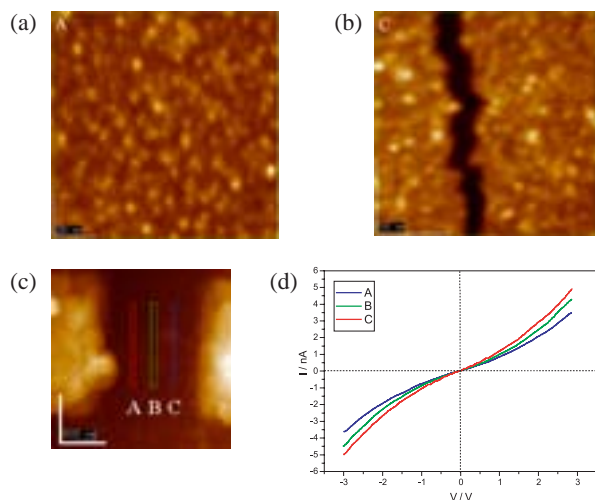


**Figure 1.** (a) and (b) Tapping mode AFM topographies of the self-assembled film of **14** on the micro-gap gold electrodes corresponding to the areas marked in (c). (d) *I-V* curves with different separations between cantilever and brass substrate by using contacting mode AFM.

### IX-A-4 Simple Preparation Method for Supramolecular Porphyrin Arrays on Mica Using Air/Water Interface

SATO, Hirokazu<sup>1</sup>; TSUTSUMI, Osamu<sup>1</sup>; TAKEDA, Kazuyoshi<sup>1</sup>; TANAKA, Hirofumi<sup>2</sup>; OGAWA, Takuji<sup>2</sup>  
(<sup>1</sup>Ebara Research Co.; <sup>2</sup>IMS, JST)

[Jpn. J. Appl. Phys. in press (2005)]

The fabrication of supramolecular porphyrin arrays on the surface of a mica substrate is demonstrated. The supramolecular structures are prepared at the air/water interface from a dilute solution of porphyrin dimer and bidentate ligand and then transferred to mica by using the conventional Langmuir-Blodgett method. Isolated wire-like structures and networks of structures are observed by atomic force microscopy. From the analysis of the height histogram and average width, these structures are considered to be side-by-side arrangements of supramolecular chains of porphyrin dimer and bidentate ligand. By changing the ligand molecule, we demonstrate that the configuration of the supramolecular structure can be controlled.

### IX-A-5 Novel Photochemical Synthesis of Pentacene and Its Derivatives

YAMADA, Hiroko<sup>1</sup>; YAMASHITA, Yuko<sup>1</sup>; KIKUCHI, Makoto<sup>1</sup>; WATANABE, Hikaru<sup>1</sup>; OKUJIMA, Tetsuo<sup>1</sup>; UNO, Hidemitsu<sup>2</sup>; OGAWA, Takuji<sup>3</sup>; OHARA, Keishi<sup>1</sup>; MUKAI, Kazuo<sup>1</sup>; ONO, Noboru<sup>1</sup>  
(<sup>1</sup>Ehime Univ.; <sup>2</sup>Ehime Univ., JST; <sup>3</sup>IMS, JST)

[Chem. Eur. J. 11, 6212 (2005)]

A novel -diketone precursor of pentacene, 6,13-dihydro-6,13-ethanopentacene-15,16-dione, was prepared and converted successfully to pentacene in 74% yield by photolysis of the precursor in toluene: Irradiation of the diketone solution in toluene with light of 460 nm under an Ar atmosphere caused the solution to change from yellow to fluorescent orange-pink within a few minutes, after which, purple precipitates appeared. After 35 min, the solution changed to colorless and the purple precipitates were filtered to give pentacene in 74% yield. By contrast, in the presence of oxygen, the color of the solution changed from yellow to pale yellow, and only 6,13-endoperoxide of pentacene was quantitatively obtained. The rate of the reaction upon photolysis was measured by observing the decay of *n*-\* absorption of the precursor at 460 nm, and was found to be similar in both the presence and absence of oxygen. Therefore, the photoreaction of the -diketone precursor seemed to occur *via* the singlet excited state. Because the T-T absorption of pentacene was observed upon

photolysis of the precursor in the nanosecond transient absorption measurement under an Ar atmosphere, the excited triplet state of the pentacene generated singlet oxygen by sensitization, and it reacted with the ground-state pentacene to give the 6,13-endoperoxide. The diketone deposited on glass was also converted successfully to pentacene film by photoirradiation. In addition, diketone precursors of a mixture of 2,8- and 2,9-dibromopentacene and 2,6-trianthrylene were also prepared and their photoconversion was performed.

### IX-A-6 Porphyrin Molecules Working as Nanodevice on Single-Walled Carbon Nanotube Wiring

TANAKA, Hirofumi<sup>1</sup>; YAJIMA, Takashi;  
MATSUMOTO, Takuya<sup>2</sup>; OTSUKA, Yoichi<sup>2</sup>;  
OGAWA, Takuji<sup>1</sup>  
(<sup>1</sup>IMS, JST; <sup>2</sup>Osaka Univ., JST)

[*Adv. Mater.* in press]

For the future development of molecular electronics, we should construct nanosized molecular devices placed on nanowiring. To obtain high-quality devices composed of a few molecules, the wiring and the device should be connected well to maintain a constant interface. For this purpose, a single-walled carbon nanotube (SWNT)/porphyrin complex was prepared and then its electronic property was investigated while observing a topographic image using point-contact current imaging atomic force microscopy (PCI-AFM). Using PCI-AFM, we can measure the current along the long axis of the wiring by which the quality of the device in the circuit can be determined. The *I-V* curves were asymmetric with respect to the origin where an aggregate of several porphyrin molecules was absorbed, while they were symmetric without them. This means the porphyrin aggregation works as a rectification device on SWNT wiring. This is the first study which proves the electron property of a few porphyrin molecules absorbed on SWNT.

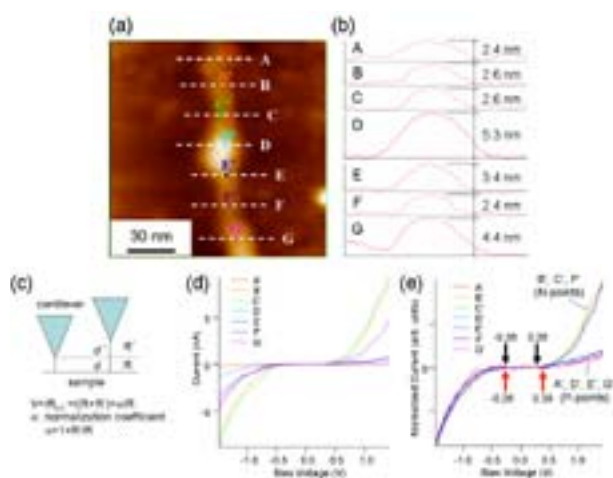


**Figure 1.** (a) Topographic image of **BPP-Zn** absorbed on SWNT electrode. The *I-V* measurement was performed at points A'-G'. (b) Cross section of each line in (a). (c) Relation between a tunnel resistance and a distance of sample and cantilever. (d) *I-V* curves obtained at each point. (e) The *I-V* curves were normalized at  $-1.5$  V. All curves are coincident below  $0$  V. *I-V* curves are classified into two types over  $0$  V. One is symmetrical with respect to the origin where porphyrin is absorbed and another is asymmetrical where no porphyrin is absorbed. Two types of arrow indicate the band edges (BE) of the objects. Black and red arrows indicate the BE of the object for N-points and P-points, respectively.

### IX-A-7 Electronic Properties of Single-Walled Carbon Nanotube/Porphyrin Polymer Complex Measured by Point-Contact Current Imaging Atomic Force Microscopy

TANAKA, Hirofumi<sup>1</sup>; YAJIMA, Takashi; KAWAO, Masahiro<sup>2</sup>; OGAWA, Takuji<sup>1</sup>  
(<sup>1</sup>IMS, JST; <sup>2</sup>SOKENDAI, IMS)

[*J. Nanosci. Nanotechnol.* in press]

The electronic properties of a porphyrin polymer wire absorbed on a single-walled carbon nanotube (SWNT) were investigated. Current-voltage (*I-V*) curves were measured simultaneously along with topographic observations using point-contact current imaging atomic force microscopy (PCI-AFM). *I-V* curves taken at the location of porphyrin polymer wire absorption were asymmetric with respect to the origin, while they were symmetric in the absence of a porphyrin polymer wire. The electron conduction mechanism of the porphyrin on the SWNT was similar to the case of SWNT/ 5,15-Bis-pentylporphyrinato zinc(II) complex in our recent work.

### IX-A-8 Preparation of Very Reactive Thiol-Protected Gold Nanoparticles: Revisiting the Brust-Schiffrin Method

ARAKI, Koiti<sup>1</sup>; MIZUGUCHI, Eisuke<sup>2</sup>; TANAKA, Hirofumi;  
OGAWA, Takuji  
(<sup>1</sup>SaoPaulo Univ.; <sup>2</sup>Ehime Univ.)

[*J. Nanosci. Nanotechnol.* in press]

Metal nanoparticles have attracted great interest in nanoscience and nanotechnology because of the many possibilities envisaged by the bottom-up approach since they possess unique optical, electrical, bonding and catalytic properties. Among them, the gold clusters are the most stable and extensively studied materials, and have been proposed for applications such as in photoelectrochemical devices, drug delivery systems and chemical and immunosensors. In all these cases, the properties of the materials should be adjusted by anchoring molecular species with suitable properties on the surface. In this sense, the availability of easily functionalizable and stable starting materials is an important aspect since there is a myriad of molecular species and other materials that can be combined with for the development of new inorganic-organic hybrid nanomaterials and applications.

The higher stability and possibility to isolate a solid that can be repeatedly isolated and redissolved in common organic solvents without decomposition and the possibility to treat them just as another organic molecular species is very convenient. However, there is a drawback for the widespread use of such a thiol protected materials: the sluggishness of the functionalization reaction by substitution of the protecting species, which can take more than a day to proceed until completion. The use of conventional organic chemistry on  $\omega$ -functionalized protecting molecules is also tedious and hampers the preparation of organic-inorganic hybrid nanomaterials, for example by coordinative layer-by-layer assembly. Accordingly, we revisited the Brust-Schiffrin method envisaging the preparation of substitutionally reactive but stable enough thiol protected gold nanoparticles to isolate them as a solid.

## IX-B Development of Organic Semiconductors for Molecular Thin-Film Devices

Organic light-emitting diodes (OLEDs) and organic field-effect transistors (OFETs) based on  $\pi$ -conjugated oligomers have been extensively studied as molecular thin-film devices. Organic semiconductors with low injection barriers and high mobilities are required for highly efficient OLEDs and OFETs. Radical cations or anions of an organic semiconductor have to be generated easily at the interface with an electrode (or a dielectric), and holes or electrons must move fast in the semiconducting layer. Compared with organic p-type semiconductors, organic n-type semiconductors for practical use are few and rather difficult to develop. Recently, we found that perfluorinated aromatic compounds are efficient n-type semiconductors for OLEDs and OFETs.

### IX-B-1 Organic Thin-Film Transistors with High Electron Mobility Based on Perfluoropentacene

INOUE, Youji<sup>1</sup>; SAKAMOTO, Youichi; SUZUKI, Toshiyasu; KOBAYASHI, Masafumi<sup>2</sup>; GAO, Yuan<sup>2</sup>; TOKITO, Shizuo<sup>1</sup>

(<sup>1</sup>NHK Sci. Tech. Res. Labs.; <sup>2</sup>Kanto Denka Kogyo)

[*Jpn. J. Appl. Phys., Part 1* **44**, 3663–3668 (2005)]

We report on n-channel organic thin-film transistors (OTFTs) based on the novel n-type organic semiconductor, perfluoropentacene. The transistor exhibits excellent electrical characteristics, with a high electron mobility of  $0.22 \text{ cm}^2/(\text{V s})$  and a good current on/off ratio of  $10^5$ . The electron mobility is comparable to the hole mobility of a pentacene OTFT. By combining the n-type perfluoropentacene and the p-type pentacene, we have fabricated ambipolar OTFTs and complementary inverter circuits. The OTFTs with heterostructures of the p- and n-type organic semiconductors can operate as an ambipolar device with high electron and hole mobilities of  $0.042$  and  $0.041 \text{ cm}^2/(\text{V s})$ . The complementary inverter using an n-channel perfluoropentacene OTFT and a p-channel pentacene OTFT exhibits excellent transfer characteristics with a voltage gain of 45. A complementary inverter using the ambipolar OTFTs is also demonstrated.

### IX-B-2 Organic Light-Emitting Diodes Using Multifunctional Phosphorescent with Iridium-Complex Core and Charge-Transporting Dendrons

TSUZUKI, Toshimitsu<sup>1</sup>; SHIRASAWA, Nobuhiko; SUZUKI, Toshiyasu; TOKITO, Shizuo<sup>1</sup>

(<sup>1</sup>NHK Sci. Tech. Res. Labs.)

[*Jpn. J. Appl. Phys., Part 1* **44**, 4151–4154 (2005)]

We report a novel class of light-emitting materials for use in organic light-emitting diodes (OLEDs): multifunctional phosphorescent dendrimers that have a phosphorescent core and dendrons based on charge-transporting building blocks. We synthesized first-generation and second-generation dendrimers consisting of a fac-tris(2-phenylpyridine)iridium [Ir(ppy)<sub>3</sub>] core and hole-transporting phenylcarbazole-based dendrons. Smooth amorphous films of these dendrimers were formed by spin-coating them from solutions. The OLEDs using the

dendrimer exhibited bright green or yellowish-green emission from the Ir(ppy)<sub>3</sub> core. The OLEDs using the film containing a mixture of the dendrimer and an electron-transporting material exhibited higher efficiency than those using the neat dendrimer film. The external quantum efficiency of OLEDs using the film containing a mixture of the first-generation dendrimer and an electron-transporting material was as high as 7.6%.

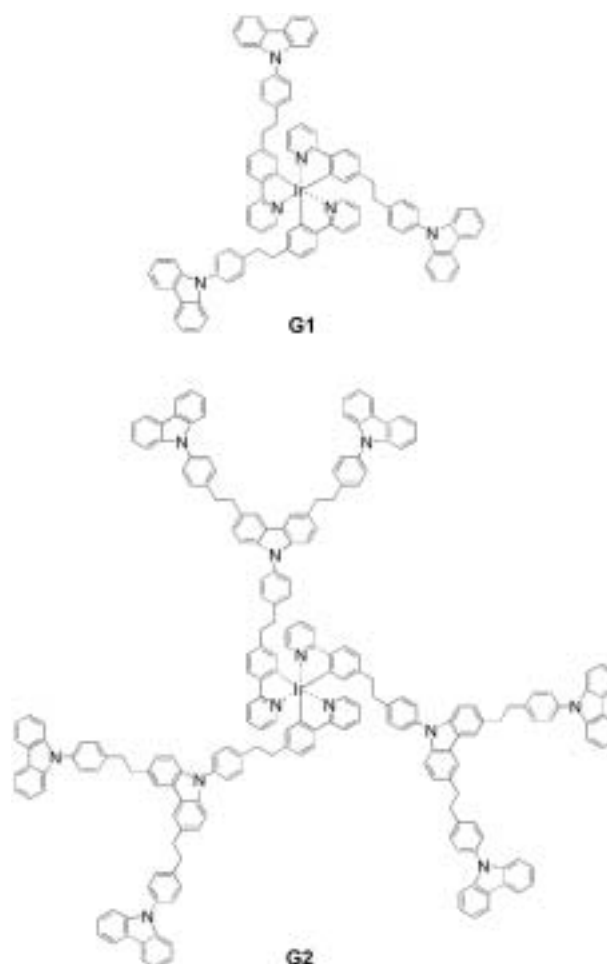


Figure 1. Structures of iridium complexes.

## IX-C Field-Effect Transistors with Organic Semiconductors

Considerable attention has recently focused on organic field-effect transistors (OFET) because of their potential use in low-cost flexible electronic devices. We have studied output characteristics of OFET devices based on newly synthesized organic compounds with novel device structures.

### IX-C-1 Preparation of Organic Light-Emitting Field-Effect Transistors with Asymmetric Electrodes

SAKANOUE, Tomo<sup>1</sup>; FUJIWARA, Eiichi;  
YAMADA, Ryo; TADA, Hirokazu  
(<sup>1</sup>SOKENDAI)

[*Chem. Lett.* **34**, 494–495 (2005)]

Light-emitting field-effect transistors (LEFET) based on poly [2-methoxy-5-(2-ethylhexoxy)-1,4-phenylenevinylene](MEH-PPV) were prepared with asymmetric electrodes of a Au/Cr source and an Al drain on a SiO<sub>2</sub> gate insulator (600 nm) through twice of photolithography and lift-off techniques (see Figure 1). The light emission was observed when the gate voltages increased above -40 V at the drain voltage of -100 V. The luminous efficiency of the devices was significantly improved comparing to those with conventional electrodes of Au/Cr.

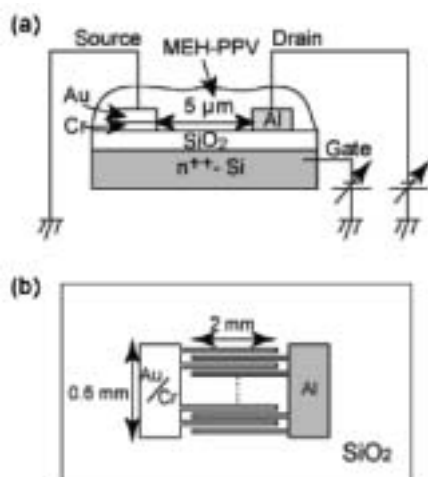


**Figure 1.** Schematic views of the LEFET with asymmetric Au/Cr-Al electrodes. (a) Side view of the device. (b) Top view of the FET substrate.

### IX-C-2 Field-Effect Transistors Based on Single-Crystalline Wires of Bis-(1, 2, 5-Thiadiazolo)-*p*-Quinobis(1, 3-Dithiole)

FUJIWARA, Eiichi; TAKADA, Masaki<sup>1</sup>;  
YAMASHITA, Yoshiro<sup>2</sup>; TADA, Hirokazu  
(<sup>1</sup>SOKENDAI; <sup>2</sup>Tokyo Inst. Tech.)

[*Jpn. J. Appl. Phys.* **44**, L82–L84 (2005)]

We prepared single-crystalline wires of bis(1, 2, 5-thiadiazolo)-*p*-quinobis(1, 3-dithiole), whose ends were anchored to the drain and source electrodes of bottom-contact-type field-effect transistors. Figure 1 shows the temperature dependence of carrier mobility in the range from 5 K to 330 K. The tunnel transport was found to be dominant at  $T < 30$  K. Thermally activated hopping behavior was observed in the temperature range from 30 K to 200 K. The mobility decreased with increasing temperature at  $T > 200$  K, indicating that phonon scattering governs carrier transport in single-crystalline wires.

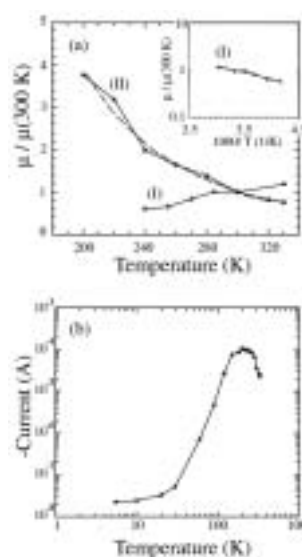


**Figure 1.** (a) Temperature dependences of the field-effect mobilities of densely packed grains (I) and crystalline wires (II). Each curve is normalized by the mobility at 300 K. Dashed line shows the  $T^{-3}$  fitting curve for  $x = 3$ . Inset shows Arrhenius's plot of curve (I). (b) Temperature dependence of the drain current of BTQBT wires. The drain and gate voltages were -50 V and -30 V, respectively.

## IX-D Molecular Assemblies on Silicon Surfaces via Silicon–Carbon Covalent Bonds

Preparation of molecular assemblies on inorganic semiconductors such as silicon and germanium has received a growing interest because of their potential application to stable resist for nano-patterning. We have prepared organic monolayers on silicon by wet process and studied film structures with IR.

### IX-D-1 Characterization of Molecular Assemblies on Silicon Surfaces by Attenuated Total Reflectance Infrared Spectroscopy

ARA, Masato<sup>1</sup>; YAMADA, Ryo; TADA, Hirokazu  
(<sup>1</sup>SOKENDAI)

[*Thin Solid Films* in press]

Alkyl monolayers anchored to Si(111) were prepared in diluted and neat 1-alkene by thermal reaction. Monolayers prepared were investigated by attenuated total reflectance infrared spectroscopy. It was found that alkyl chains in the monolayers anchored to Si(111) had an all-trans conformation. The rate of reaction between 1-alkene and hydrogen-terminated silicon remarkably depended on the concentration of 1-alkene as shown in Figure 1. However, monolayers prepared in diluted 1-

alkene were identical with that prepared in neat 1-alkene.

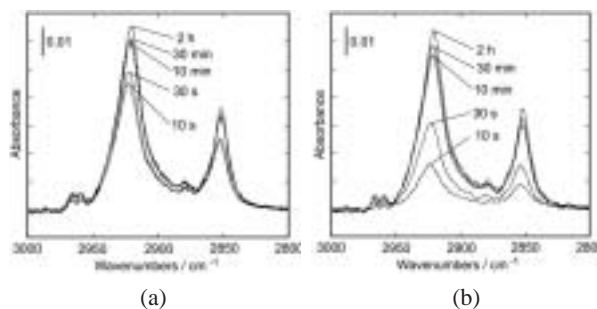


**Figure 1.** ATR spectra of C12 monolayers prepared in neat 1-dodecene (a) and those prepared in diluted 1-dodecene (b) with a p-polarized configuration, respectively. Reaction was carried out for 10 s, 30 s, 10 min, 30 min, and 2 h.

## IX-E Low Temperature Scanning Tunneling Microscopy and Spectroscopy of Organic Molecules on Metal Surfaces

The electronic structure of molecules adsorbed by metal surfaces is of growing interest in the field not only of surface science but also of molecular-scale electronic devices. Scanning tunneling microscopy and spectroscopy are useful to investigate molecular arrangements and electronic structure with atomic resolution. We have prepared epitaxial films of phthalocyanine molecules on clean metal surfaces and studies their structures by scanning tunneling microscopy and spectroscopy at low temperature.

### IX-E-1 Scanning Tunneling Microscopy and Spectroscopy of Phthalocyanine Molecules on Metal Surfaces

TAKADA, Masaki<sup>1</sup>; TADA, Hirokazu  
(<sup>1</sup>SOKENDAI)

[*Jpn. J. Appl. Phys.* **44**, 5332–5335 (2005)]

We studied the electronic structure of cobalt-phthalocyanine (CoPc) molecules on Au(111) and Cu(100) surfaces by scanning tunneling microscopy and

spectroscopy at 5 K. In the differential conductance ( $dI/dV$ ) spectra as shown in Figure 1, there were some peaks related to the highest occupied molecular orbital (HOMO), the lowest unoccupied MO (LUMO) and the d-orbitals of the Co atom. CoPc molecules on the Cu(100) surface had new electronic states between the peaks related to HOMO and LUMO, while those on the Au(111) surface did not show additional peaks. A  $dI/dV$  image indicated that the new states were generated by the hybridization between the LUMO of molecules and the electronic states of the Cu(100) surface.

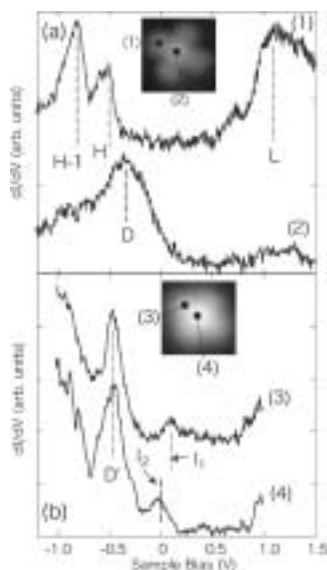


**Figure 1.** (a)  $dI/dV$  spectra of a single CoPc molecule on Au(111) surface at 5 K. (b)  $dI/dV$  spectra of a single CoPc molecule on Cu(100) surface at 5 K. Spectra (1)–(4) were measured at indicated spots on the inset images.

## IX-F Ratchet Motions of a Droplet Caused by Electrochemical Reaction of Monolayers

Control of droplet motions on small spaces is of growing interest since it leads to non-mechanical pumping systems in micro-fluidic devices. By introducing asymmetric characteristics to the surface, the droplet moves because of the imbalance of surface tensions. We found that electrochemical reactions of monolayers were used to dynamically control the surface property and the motion of the droplet.

### IX-F-1 Electrochemically Generated Wetting Gradient and Its Application for the Transport of Droplets

YAMADA, Ryo; TADA, Hirokazu

[*Langmuir* **21**, 4254–4256 (2005)]

The reversible transportation of droplets was realized by spatiotemporal control of the wetting gradient. The surface wetting was reversibly regulated by using electrochemical reactions of the ferrocenyl (Fc) alkanethiol monolayer and application of the in-plane bias voltage to the substrate as shown in Figure 1. The back-and-forth motion of the wetting boundary, where the surface changed from wetting to repulsive, sequentially caused a droplet unidirectional spreading and shrinking on the surface. These unidirectional motions resulted in the net transport of the droplet in inchworm-like manner as shown in Figure 2. The droplet moved backward when the direction of the in-plane bias voltage was reversed.

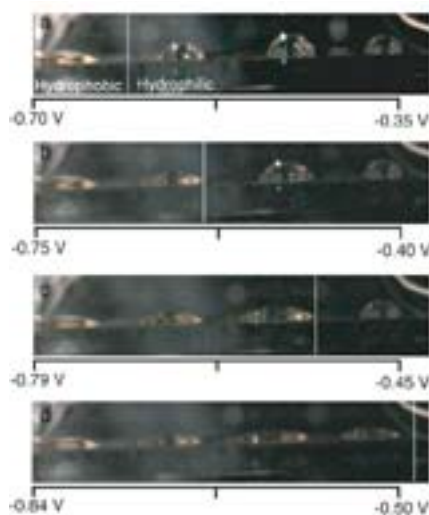


**Figure 1.** Photographs of nitrobenzene droplets.  $V_{bias}$  was fixed at 0.35 V and  $E_{offset}$  was shifted (a–d). Line in the photograph represents the position of the wetting boundary estimated from the shape of the droplets. Note that the current peak for  $Fc^+/Fc$  reaction was observed at *ca.*  $-0.5$  V in cyclic voltammogram.

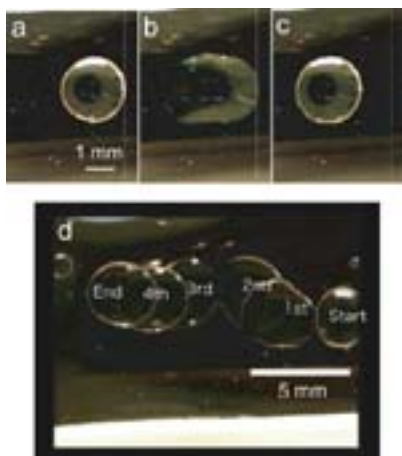


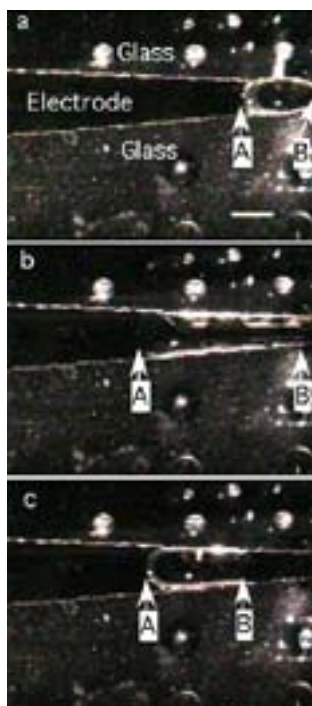
**Figure 1.** Directional deformations of the nitrobenzene droplet. The length of the scale bar in (a) is 3 mm. When the surface was changed from repulsive to wetting (a–b), the left side of the droplet (A) spread. When the surface was back to repulsive (bc), the right side of the droplet (B) shrank. These directional deformations resulted in a net transport of the droplet.

**Figure 2.** Photographs of inchworm motion of the droplet in the solution.  $E_{BIAS} = 0.5$  V.  $E_{offset} = -300$  mV (a),  $-340$  mV (b) and  $-300$  mV (c). (d) Trace of the multi-step inchworm motions of the droplet. Six photographs were superimposed.

### IX-F-2 Transport of a Droplet by Directional Deformations with Asymmetric Electrode

YAMADA, Ryo; TADA, Hirokazu

Ratchet motions of a droplet were realized by the repeated deformations of it on an asymmetric V-shaped electrode. The surface wetting of the electrode was reversibly regulated by electrochemical reactions of the ferrocenyl-alkanehiol monolayer. When the surface was changed from repulsive to wetting, the contact line of the droplet facing to the wider side advanced while the other side was almost pinned. The contact line facing to the narrower side retracted when the surface was changed from wetting to repulsive. The directional deformations of the droplet resulted in a net transport of it.



## IX-G Development of Multi-Function Integrated Macromolecules and Their Organization on Substrate Surfaces for Planar Molecular-Scale Electronics Circuits

The concept of molecular-scale electronics is now realized for individual components such as wire, diode, switch, and memory cell, but the fabrication of complete molecular-scale circuits remains challenging because of the difficulty of connecting molecular modules to one another. Molecular monolithic technology, which integrates the wiring, transistors and the required passive elements on a single macromolecule, has been proposed as a promising solution to this problem. In this project we have been trying to establish both the architecture of this novel class of macromolecules and the protocols for their purposive organization on metal/semiconductor substrate surfaces.

### IX-G-1 Step-Wised Synthesis of Multifunctional Molecular Wires for Planar Metal-Molecule-Metal Junctions

TANAKA, Shoji

A series of 1–10 nm long building blocks (**1-4**) have been prepared. We have already developed i) “insulated molecular modules,” ii) “energy-gap tuning modules,” iii) “molecule-anchor modules,” and iv) “molecular junction modules” as the basic elements for multi-function integrated  $\pi$ -conjugated macromolecules. The building blocks **1-4** are widely applicable to assemble these functional modules in a single molecule. For example, a series of linear macromolecules (**5-6**), specifically designed for the systematic investigation of electron conduction in molecular wires, have been prepared easily from these blocks and modules in a few steps.

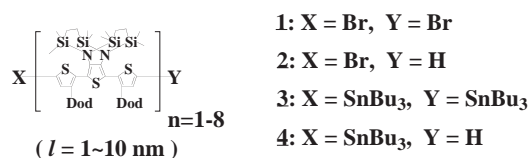
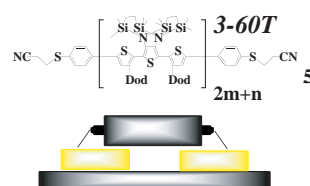
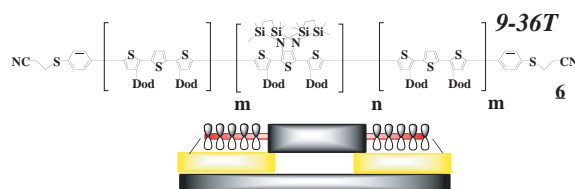


**Figure 1.** Molecular structure of 1–10 nm long building blocks.



Molecular wires for alligator-clip junction ( $l = 1\text{--}25$  nm)



Molecular wires for face-to-face junction ( $l = 3\text{--}15$  nm)

**Figure 2.** Molecular structure of insulated molecular wires with anchor units.

## IX-H Heterogeneous Aquacatalysis

Catalytic organic transformations under mild, safe, and green conditions is an important goal in synthetic organic chemistry. We recently reported that several palladium- and rhodium-catalyzed reactions, including  $\pi$ -allylic substitution, carbonylation, the Heck reaction, Suzuki-Miyaura cross-coupling, hydroformylation, cyclotrimerization of alkynes, and Michael-type addition of arylboronic acids, *etc.*, took place in water by use of metal-phosphine complexes anchored on to an amphiphilic polystyrene-poly(ethylene glycol) graft copolymer (PS-PEG) resin where the advantages of both aqueous- and heterogeneous-switching of a given catalytic transformation were combined in one system. Here we wish to report our progress in this subject.

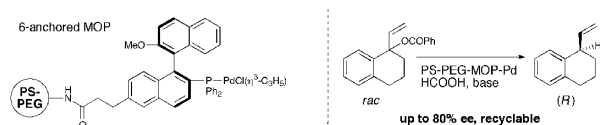
### IX-H-1 PS-PEG Resin-Supported Palladium-MOP Complexes. Application in Asymmetric $\pi$ -Allylic Reduction

[*Org. Lett.* 7, 291–293 (2005)]

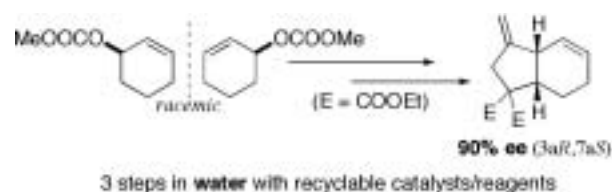
UOZUMI, Yasuhiro; HOCKE, Heiko

[*Tetrahedron* 60, 9297–9306 (2004)]

Homochiral palladium complexes of polymeric 2', 6-, and 6'-anchored 2-diphenylphosphino-1,1'-binaphthyl (MOP) ligands were prepared on polystyrene-poly(ethylene glycol) (PS-PEG) resin. The PS-PEG resin-supported palladium-MOP complexes exhibited high catalytic activity, stereoselectivity (up to 80% *ee*), and recyclability (6 times) in the asymmetric allylic reduction of 1-vinyl-1,2,3,4-tetrahydronaphth-1-yl benzoate to give 1-vinyl-1,2,3,4-tetrahydronaphthalene.



Cycloisomerization of 1,6-enynes proceeded smoothly in water under heterogeneous conditions in the presence of a palladium complex supported on polystyrene-poly(ethylene glycol) copolymer resin to give the corresponding cyclopentanes with high level of chemical greenness. Multi-step asymmetric synthesis of a hydrindane framework was achieved via palladium-catalyzed asymmetric  $\pi$ -allylic alkylation, propargylation, and cycloisomerization of 1,6-enynes, where all three steps were performed in water with recyclable polymeric catalysts.

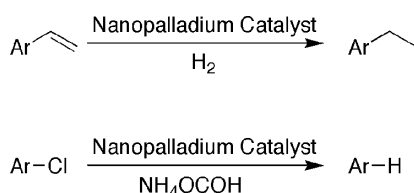


### IX-H-2 Hydrogenation and Dehalogenation under Aqueous Conditions with an Amphiphilic Polymer-Supported Nanopalladium Catalyst

NAKAO, Ryu; RHEE, Hakjune; UOZUMI, Yasuhiro

[*Org. Lett.* 7, 163–165 (2005)]

An amphiphilic polystyrene-poly(ethylene glycol) resin-supported nanopalladium particle catalyzed hydrogenation of olefins and hydrodechlorination of chloroarenes under aqueous conditions.



### IX-H-3 Cycloisomerization of 1,6-Enynes: Asymmetric Multi-Step Preparation of a Hydrindane Framework in Water with Polymeric Catalysts

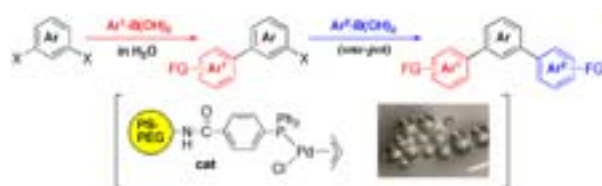
NAKAI, Yasushi; UOZUMI, Yasuhiro

### IX-H-4 Controlled Monoarylation of Dibromoarenes in Water with a Polymeric Palladium Catalyst

UOZUMI, Yasuhiro; KIKUCHI, Makoto

[*Synlett* 1775–1778 (2005)]

A highly selective monoarylation of dibromoarenes was performed via the Suzuki-Miyaura cross-coupling with arylboronic acids with an amphiphilic polystyrene-poly(ethylene glycol) (PS-PEG) resin-supported phosphine-palladium complex in water under heterogeneous conditions to give bromobiaryls in high yields. Introduction of two different aryl groups on a aromatic moiety was achieved in a one-pot reaction by successive addition of two kinds of arylboronic acids under similar conditions. The polymeric palladium catalyst can be readily recovered and recycled.



## IX-I Development of New Nanomaterials as Components in Advanced Molecular Systems

Nanometer-sized materials exhibit unique electronic behavior. In the quest of advanced redox catalysis, we are currently interested in combining nanometer-sized materials into molecular redox systems. As a basic architecture, composites of organic molecules and gold nanoparticles were synthesized and molecular dynamic simulations were carried out to predict the solution structures.

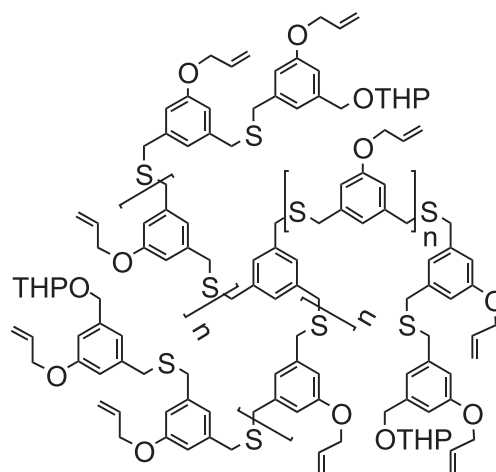
### IX-I-1 Gold Nanoparticles Stabilized by Tripod Thioether Oligomers: Synthesis and Molecular Dynamics Studies

HOSOKAWA, Youichi; MAKI, Suguru; NAGATA, Toshi

[*Bull. Chem. Soc. Jpn.* in press (2005)]

Gold nanoparticles (1.5–1.7 nm) were prepared by use of three tripod thioether oligomers (TTOs) as stabilizing molecules shown in Figure 1. The ICP-AES analyses of these TTO/Au<sub>n</sub> composites revealed the number of protecting molecules per nanoparticles as 25±19, 23±21, and 10±6. On the other hand, the molecular models suggested that the TTOs were of comparable sizes with the sizes of nanoparticles. In order to account for this discrepancy, we carried out molecular dynamic simulations of the TTO/Au<sub>n</sub> composites. The interaction parameters between organic molecules and the gold surface were newly developed so that they reproduced the adsorption enthalpies of small sulfur-containing molecules on the Au(111) surface. By use of these parameters, the self-assembly process of TTO molecules on the Au<sub>147</sub> surface was simulated in chloroform solvent. Figure 2 shows the typical results from a single run, in which 16 TTO molecules (**1a**) and an Au<sub>147</sub> nanoparticle (a cuboctahedral structure; diameter 1.7 nm) were placed in a box of CHCl<sub>3</sub> with dimensions 112.2×96.3×97.7 Å<sup>3</sup>. The surface of the gold nanoparticle was completely covered with three TTO molecules. Although it is not impossible to accommodate more than 20 **1a**'s around the surface of a gold nanoparticle, the more appropriate model would be coexistence of free, unbound **1a** molecules and gold nanoparticles covered with a small number of **1a**. The free and bound **1a** molecules should be in dynamic equilibrium in CHCl<sub>3</sub> solutions, as suggested

by the <sup>1</sup>H NMR spectra which showed only one set of slightly broadened signals.



**1a**:  $n = 1$ , **1b**:  $n = 3$ , **1c**:  $n = 5$

**Figure 1.** The tripod thioether oligomers used in this study.

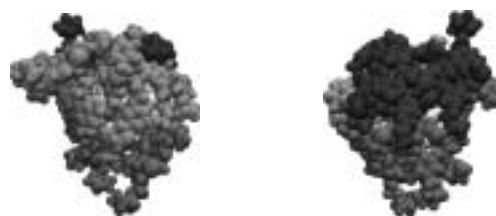


**Figure 2.** A snapshot structure from the **1a**<sub>16</sub>/Au<sub>147</sub> simulation, in which three **1a** molecules are adsorbed on the Au<sub>147</sub> surface. The space-filling views from two opposite directions are shown. The gold nanoparticle and the three different **1a** molecules are denoted in white color and three different levels of gray colors, respectively.

## IX-J Designing Artificial Photosynthesis at Molecular Dimensions

Photosynthesis is one of the finest piece of molecular machinery that Nature has ever created. Its ultrafast electron transfer and following well-organized sequence of chemical transformation have been, and will continue to be, challenging goals for molecular scientists. Our ultimate goal is to design artificial molecular systems that effect multiple chemical reactions triggered by light on the basis of molecular rationale.

### IX-J-1 Electrochemical Properties of Ferrocene-Dendrimer-Porphyrins

KIKUZAWA, Yoshihiro; NAGATA, Toshi

Synthesis of the ferrocene-dendrimer-porphyrins (Figure 1) was already reported in previous Annual Reviews. Figure 2 shows the differential pulse voltammograms (DPV) of  $G_n(\text{Fc})_m\text{-ZnP}$ , together with the reference compounds **Bn-ZnP** and **Fc-ZnP**, in  $\text{CH}_2\text{Cl}_2/0.1 \text{ mol/dm}^3 \text{ Bu}_4\text{NClO}_4$ . The ferrocene-dendrimer-porphyrin compounds showed three oxidation peaks at 0.2, 0.5 and 0.7 V (vs  $\text{FcCp}_2/\text{FcCp}_2^+$ ), which were assigned as the oxidation of the ferrocenyl groups, and the first and second oxidation of the porphyrin. Figure 3 shows the plots of  $i_{\text{max}}$  (the peak height) versus  $\Delta t^{-1/2}$  ( $\Delta t$  is the pulse width) for the first two oxidation peaks of **G3(Fc)<sub>14</sub>-ZnP**. The values for peak II showed good linearity, whereas those for peak I showed pronounced deviation from linearity. These results indicate that the electron transfer for the first oxidation (peak I) is slow in the electrochemical timescale. This slow kinetics can be attributed to the reorganization of the supporting electrolyte during the multiple electron transfer of the ferrocene-dendrimer redox pool.

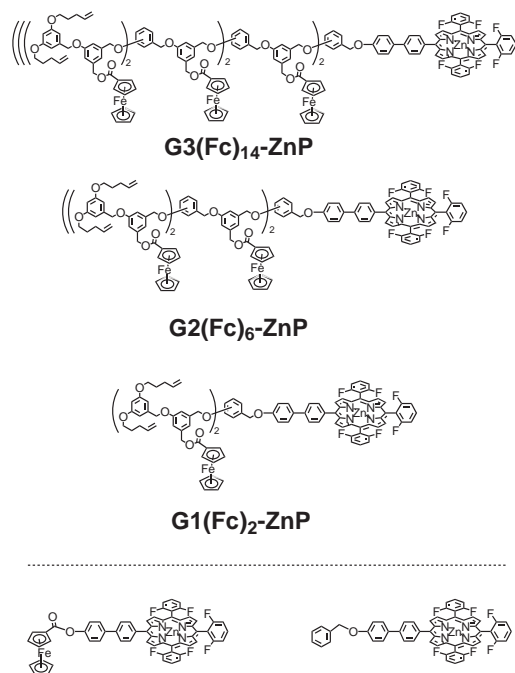


**Figure 1.** The structure of the ferrocene-dendrimer-linked porphyrins.

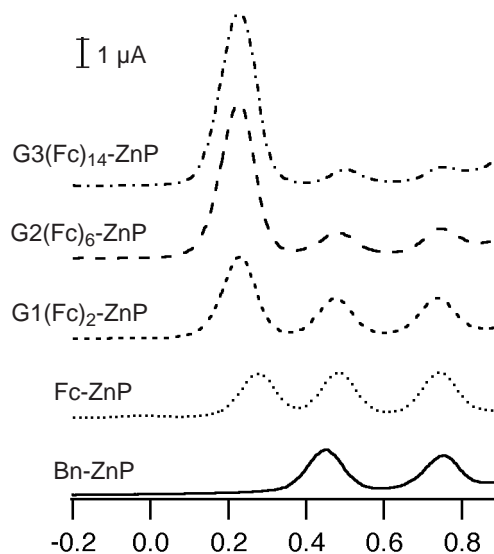


**Figure 2.** The differential pulse voltammograms of the ferrocene-dendrimer-porphyrins.

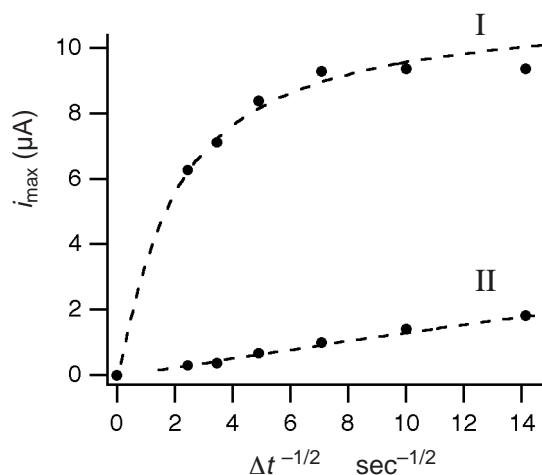


**Figure 3.** The  $i_{\text{max}}-\Delta t^{-1/2}$  plots of the first two oxidation peaks of **G3(Fc)<sub>14</sub>-ZnP**.

### IX-K Development of New Metal Complexes as Redox Catalysts

Redox catalysis is an important field of chemistry which translates a flow of electron into chemical transformation. It is also one of the requisites for artificial photosynthesis. This project of ours aims at developing new metal complexes that perform redox catalysis at low overpotential. Currently we are focusing our attention to the development of a series of cobalt phosphine complexes as possible catalysts for electrochemical reductions.

### IX-K-1 Synthesis, Structure and Electrochemistry of New Cobalt Complexes with Cyclopentadienyl and Bidentate Ligands

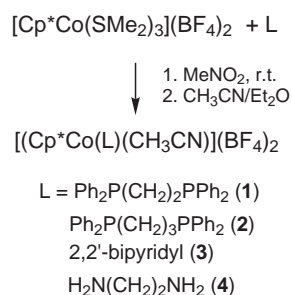
NAGASAWA, Takayuki; NAGATA, Toshi

Low-valent cobalt complexes are interesting candidates for electrocatalytic reductions. Herein we report the synthesis, structure, and electrochemistry a series of cobalt complexes with general formula  $[\text{Cp}^*\text{Co}(\text{L})(\text{S})]^{2+}$ , where  $\text{Cp}^*$  is pentamethylcyclopentadienyl anion, L is a bidentate ligand and S is an exchangeable monodentate ligand.

The key intermediate compound,  $[\text{Cp}^*\text{Co}(\text{SMe}_2)_3](\text{BF}_4)_2$ , was prepared from  $\text{Cp}^*\text{Co}(\text{CO})_2$  by a similar method as the Cp analog reported by Kuhn. The reaction of this compound with a bidentate ligand in  $\text{CH}_3\text{NO}_2$ , followed by treatment with  $\text{CH}_3\text{CN}/\text{Et}_2\text{O}$ , gave a crystalline product  $[\text{Cp}^*\text{Co}(\text{L})(\text{CH}_3\text{CN})](\text{BF}_4)_2$  in 80–90% yield (Scheme 1). The X-ray structure of **2** (L = dppp) is shown in Figure 1, which shows typical octahedral coordination of the Co(III) center. The cyclic voltammograms in  $\text{CH}_3\text{CN}$  showed two reversible waves corresponding to the Co(III)/Co(II) and Co(II)/Co(I) redox couples (Table 1).

**Table 1.** The reversible half-wave potentials of **1-4** in  $\text{CH}_3\text{CN}/\text{Bu}_4\text{NClO}_4$ .

	$E_{1/2}(\text{V vs. Cp}_2\text{Fe/Cp}_2\text{Fe}^+)$	
	Co(III)/Co(II)	Co(II)/Co(I)
<b>1</b>	-0.61	-1.13
<b>2</b>	-0.56	-1.26
<b>3</b>	-0.82	-1.15
<b>4</b>	-0.98	-2.25



**Scheme 1.** Synthesis of the cobalt complexes.

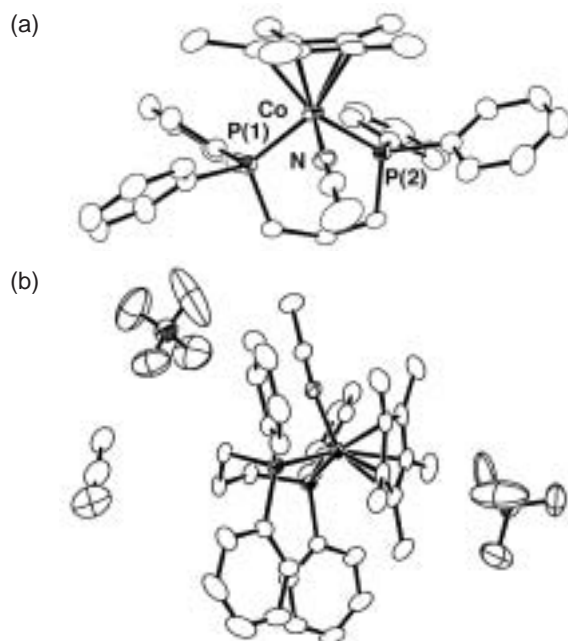


**Figure 1.** The ORTEP drawings of (a) the cationic part, and (b) the asymmetric unit of **2**.

## IX-L Photochemistry on Well-Defined Surfaces

Upon the irradiation of light in the wavelength range from visible to ultraviolet, a number of adsorbed molecules on metal surfaces reveal variety of photochemical processes, including photo-stimulated desorption, rearrangement of adsorbed states, photodissociation, and photo-initiated reactions with coadsorbates. A central and fundamental question in the surface photochemistry is to clarify how adsorbate-substrate systems are excited by photon irradiation. In addition, since photo-initiated reactions can be induced without any thermal activation of reactants, they may provide good opportunities for studying a new class of surface reactions that may not be induced thermally. We have studied photochemistry of various adsorption systems on well-defined metal and semiconductor surfaces mainly by temperature-programmed desorption (TPD), infrared reflection absorption spectroscopy (IRAS), x-ray photoelectron spectroscopy (XPS), work function measurements, and angular-resolved time-of-flight (TOF) mass spectrometry of photodesorbed species associated with pulsed laser irradiation. In this year, the photochemistry of cyclic alkane on Pt(111) and Cu(111) surfaces was studied mainly by TPD, XPS, and IRAS.

### IX-L-1 Photochemistry of Cyclohexane on Cu(111)

**YAMAGUCHI, Dai; MATSUMOTO, Taketoshi;**  
**WATANABE, Kazuya; TAKAGI, Noriaki<sup>1</sup>;**  
**MATSUMOTO, Yoshiyasu**  
*(<sup>1</sup>SOKENDAI and Univ. Tokyo)*

[*Phys. Chem. Chem. Phys.* submitted]

The photochemistry of cyclohexane on Cu(111) and its excitation mechanism have been studied by temperature-programmed desorption, ultraviolet and X-ray photoelectron spectroscopy. Cyclohexane weakly adsorbed on Cu(111) has been known to show a broadened and redshifted CH stretching band, *i.e.*, CH vibrational mode softening. Although no dehydrogenation takes place thermally on this surface and by the irradiation

of photons at 5.0 eV, adsorbed cyclohexane is dissociated to cyclohexyl and hydrogen by the irradiation of photons at 6.4 eV. This is a marked contrast to cyclohexane in the gas phase where the onset of absorption is located at 7 eV. When the surface irradiated by 6.4-eV photons is further annealed, cyclohexyl is dehydrogenated to form cyclohexene that desorbs at 230 K. The systematic measurements of photochemical cross sections at 6.4 eV with linearly polarized light as a function of incident angle indicate that the electronic transition from the highest occupied band of cyclohexane to a partially occupied hybridized band near the Fermi level is responsible for the photochemistry. The hybridized band is formed by the interactions between the electronic states of cyclohexane and the metal substrate. The role of the hybridized band in the photochemistry and the CH vibrational mode softening is discussed.

## IX-M Ultrafast Dynamics at Well-Defined Surfaces

To understand the mechanism of surface photochemistry, it is vital to know how photoinduced electronic excitation induces adsorbate nuclear motions that ultimately lead to chemical reactions. We demonstrate the real-time observations of surface phonons and adsorbate-substrate vibrational modes by fs time-resolved second harmonics generation (TRSHG). If an excitation light pulse has a duration sufficiently shorter than a period of a vibrational mode or a phonon mode, it can excite the mode with a high degree of temporal and spatial coherence. This coherent nuclear motion modulates the second-order susceptibility  $\chi^{(2)}$ . Thus, by monitoring the intensity modulation of the second harmonics (SH) generation of a probe pulse, we can observe the evolution of the coherent nuclear motion subsequent to the electronic excitation at the surfaces. This year, in particular, we have demonstrated that coherent phonon modes can be selectively excited by tailored pulse trains.

### IX-M-1 Femtosecond Wavepacket Dynamics of Cs Adsorbates on Pt(111): Coverage and Temperature Dependences

**WATANABE, Kazuya; TAKAGI, Noriaki<sup>1</sup>;**  
**MATSUMOTO, Yoshiyasu**  
*(<sup>1</sup>Univ. Tokyo)*

[*Phys. Rev. B* **71**, 085414 (9 pages) (2005)]

Femtosecond time-resolved second harmonic generation has been used to observe vibrational wavepacket

dynamics at a Cs-covered Pt(111) surface. The creation and dephasing of vibrational coherence are monitored *via* the intensity modulations in the second harmonic of probe pulses as a function of pump-probe delay. The TRSHG trace obtained from the clean surface shows an instantaneous sharp rise right after the excitation. This is followed by a fast decaying component ( $t < 1$  ps) and a slowly decaying one persistent to the longest delay ( $t = 6$  ps) of the measurements. When the surface is covered with Cs, SH signals are enhanced by about 70 times and strongly modulated waveforms are superimposed on the TRSHG traces. The oscillatory signals are found in

TRSHG signals upon the excitations at 580 and 800 nm, which are the manifestation of nuclear wavepacket dynamics on the surface. The Cs-coverage dependence studied in detail indicates that the wavepacket dynamics of Cs–Pt stretching modes and Pt surface phonon modes are responsible for the TRSHG signals. The cos-like initial phase of the oscillatory signals and the coverage dependence of the initial amplitude suggest that the vibrational coherence is associated with the resonant excitation between Cs-derived states in the quantum well of the Cs overlayer. The rate of Cs–Pt vibrational dephasing increases with the surface temperature. This behavior cannot be accounted for by the increasing contribution from hot bands of low frequency modes. Instead, pure dephasing caused by anharmonic coupling between Cs–Pt stretching and parallel modes in the Cs overlayer is likely the dominant mechanism for the vibrational dephasing.

### IX-M-2 Mode Selective Excitation of Coherent Surface Phonons on Alkali-Covered Metal Surfaces

WATANABE, Kazuya; TAKAGI, Noriaki<sup>1</sup>; MATSUMOTO, Yoshiyasu  
(<sup>1</sup>Univ. Tokyo)

[*Phys. Chem. Chem. Phys.* **7**, 2697–2700 (2005)]

We demonstrate the mode selective excitation of coherent phonons at Pt(111) surfaces covered with submonolayer cesium atoms. A burst of 150-fs laser

pulses with the repetition rate of 2.0 ~ 2.9 THz was synthesized by using a spatial-light modulator, and used for the coherent surface phonon excitation. The coherent nuclear motion was monitored by time-resolved second harmonic generation. By tuning the repetition rate, we succeeded in controlling the relative amplitude of the vibrational coherence of the Cs–Pt stretching mode (2.3 ~ 2.4 THz) to that of the Pt surface Rayleigh phonon mode (2.6 or 2.9 THz, depending on the Cs coverage).

### IX-M-3 Excitation Mechanism of Coherent Surface Phonons on Alkali-Metal Covered Surfaces

FUYUKI, Masanori<sup>1</sup>; WATANABE, Kazuya; MATSUMOTO, Taketoshi; MATSUMOTO, Yoshiyasu  
(<sup>1</sup>SOKENDAI)

We observed time-resolved second harmonic signals from the Cu(111) surface with a full monolayer of Na in ultra-high vacuum and investigated the excitation-wave-length dependence of the wave packet dynamics of the coherently excited Na–Cu stretching mode. Changing the photon energy of the pump pulse (25 fs) from 2.0 to 2.5 eV, the oscillation amplitude derived from the Na–Cu stretching motion is enhanced when the photon energy is resonant to the transitions from the ground state to image states. Thus, these measurements clearly indicate that the resonant excitation of electronic state of the adsorbate is essential for creation of the coherent surface phonons.

## IX-N Multiphoton Photoelectron Spectroscopy of Electronic States of Nano-Structured Materials on Surfaces

Electronic structure and excited state dynamics of nano-structured materials on surfaces are very important for exploring their properties, thermal reactivity and nonthermal processes including photochemistry and photo-induced charge transfer. For this purpose, we performed multiphoton photoelectron spectroscopy with the fs time resolution. In this year we applied this method to thin films of tris-(8-hydroxyquinoline) aluminum (Alq<sub>3</sub>).

### IX-N-1 The Electronic Structure and Femtosecond Electron Transfer Dynamics at Noble Metal/tris-(8-hydroxyquinoline) Aluminum Interfaces

INO, Daisuke<sup>1</sup>; WATANABE, Kazuya; TAKAGI, Noriaki<sup>2</sup>; MATSUMOTO, Yoshiyasu  
(<sup>1</sup>SOKENDAI; <sup>2</sup>Univ. Tokyo)

[*Phys. Rev. B* **71**, 115427 (10 pages) (2005)]

The electronic structures of tris-(8-hydroxyquinoline) aluminum (Alq<sub>3</sub>) on Cu(111) and Au(111) surfaces are studied by using ultraviolet photoelectron spectroscopy and two-photon photoelectron (2PPE) spectroscopy.

The work function decreases with increase of the coverage due to surface dipole of 5.1 D along the surface normal. The ionization potential from the highest occupied state 6.38 eV does not depend on the metal substrates used in this study. The anion states of Alq<sub>3</sub> adsorbed is created by photoinduced electron transfer from the metal substrates and are located at 2.85 and 3.71 eV above the Fermi level on Cu(111) and Au(111) surfaces, respectively. The full width at half maximum of the anion states is 0.2 eV on both the surfaces. Time-resolved 2PPE measurements show that the anion state created by electron transfer from the metal decays with the lifetime of 31±2 fs on Cu(111) and about three times shorter on Au(111). The angle-resolved 2PPE and the coverage dependence of the lifetime of the anion state

indicate that the electron transferred from the metal surface is localized at a molecule in the first layer. Thus, the ultrafast electron back transfer from the anion state

of  $\text{Alq}_3$  in the first layer dominates over the electron hopping to the second layer.

## IX-O Chemistry of One-Dimensional Nano-Surface Compounds Studied by Scanning Tunneling Microscopy

The fluctuating configurations of low-dimensional structures can be thermodynamically favorable at finite temperatures, because the energy gain overcomes the energy cost that accompanies local structural fluctuation. In particular, one-dimensional (1D) systems have a propensity to be sensitive to these fluctuations as described by one of the maxims of condensed matter physics, *i.e.*, one chain does not make a crystal. Thus, the dynamical formation of active species and sites by these fluctuations is a key factor in establishing a microscopic model for chemical reactions at surfaces and nano-structured compounds.

### IX-O-1 In-Situ Observation of CO Oxidation on $\text{Ag}(110)(2 \times 1)\text{-O}$ by Scanning Tunneling Microscopy: Structural Fluctuation and Catalytic Activity

NAKAGOE, Osamu<sup>1</sup>; WATANABE, Kazuya;  
TAKAGI, Noriaki<sup>2</sup>; MATSUMOTO, Yoshiyasu  
(<sup>1</sup>SOKENDAI; <sup>2</sup>Univ. Tokyo)

[*J. Phys. Chem. B* **109**, 14536–14543 (2005)]

It is well known that the adsorption of O on  $\text{Ag}(110)$  results in the formation of quasi-1D structures, AgO chains, accompanied by the mass transfer of substrate atoms.

AgO chains arrange periodically to form  $(n \times 1)$  ( $n = 2 \sim 7$ ) depending on the fractional O coverage due to repulsive inter-chain interactions. On the added-row reconstructed  $\text{Ag}(110)(n \times 1)\text{-O}$  surfaces where one-dimensional  $\text{-Ag-O-Ag-O-}$  chains arrange periodically, the clean-off reaction of O adatoms by CO was investigated using variable temperature scanning tunneling microscopy (VT-STM). Based on the in situ STM observations of the surface structure variation in the course of the reaction at various temperatures, we found that the reaction kinetics are significantly affected by the structural transition of AgO chains from a solid straight line configuration to dynamically fluctuating configurations. Below 230 K where the chains are straight, the reaction takes place only at the end of the chains, so that the reaction progresses in the zero-order kinetics with the reaction front propagating along the chain. The temperature dependence of the reaction rates yields the activation barrier of 41 kJ/mol and the pre-exponential factor of  $1.7 \times 10^3 \text{ cm}^{-2} \text{ s}^{-1}$ . At room temperature, the reaction rate is drastically accelerated when almost half of the O adatoms are eliminated and the chains start fluctuating. The dynamic formation of active sites equivalent to the end of chains upon the chain fluctuation results in the nonlinear increase of the reaction rate.

## IX-P Structures, Stabilities and Physicochemical Properties of Organometallic Hybrid Clusters

Recently, metal clusters have gained much attention because they exhibit novel physicochemical properties that are beyond the prediction made by a dimensional scaling of those of the corresponding bulk. In this regard, metal clusters protected by thiolates or stabilized by polymers are promising candidates for elementary units of nano-scale devices. Our interests are focused on the following issues on the organometallic hybrid clusters: (1) a large-scale preparation of the subnanometer-sized clusters, (2) development of size-selection method, (3) determination of chemical compositions of size-selected clusters (*i.e.* the numbers of metal atoms and organic molecules), and (4) elucidation of effect of the core size, core shape, and interaction with organic molecules on stabilities, electronic structures, and chemical properties.

### IX-P-1 Glutathione-Protected Gold Clusters Revisited: Bridging the Gap between Gold(I)-Thiolate Complexes and Thiolate-Protected Gold Nanocrystals

NEGISHI, Yuichi; NOBUSADA, Katsuyuki;  
TSUKUDA, Tatsuya

[*J. Am. Chem. Soc.* **127**, 5261–5270 (2005)]

Small gold clusters (~1 nm) protected by molecules of a tripeptide, glutathione (GSH), were prepared by reductive decomposition of Au(I)-SG polymers at a low temperature and separated into a number of fractions by polyacrylamide gel electrophoresis (PAGE). Chemical compositions of the fractionated clusters determined previously by electrospray ionization (ESI) mass spectrometry<sup>1)</sup> were reassessed by taking advantage of freshly-prepared samples, higher mass resolution and more accurate mass calibration; the nine smallest components are reassigned to Au<sub>10</sub>(SG)<sub>10</sub>, Au<sub>15</sub>(SG)<sub>13</sub>, Au<sub>18</sub>(SG)<sub>14</sub>, Au<sub>22</sub>(SG)<sub>16</sub>, Au<sub>22</sub>(SG)<sub>17</sub>, Au<sub>25</sub>(SG)<sub>18</sub>, Au<sub>29</sub>(SG)<sub>20</sub>, Au<sub>33</sub>(SG)<sub>22</sub>, and Au<sub>39</sub>(SG)<sub>24</sub>. These assignments were further confirmed by measuring the mass spectra of the isolated Au:S(*h*-G) clusters, where *h*-GSH is a *homo*-glutathione. It is proposed that a series of the isolated Au:SG clusters corresponds to kinetically trapped intermediates of the growing Au cores. The relative abundance of the isolated clusters was correlated well with the thermodynamic stabilities against unimolecular decomposition. The electronic structures of the isolated Au:SG clusters were probed by X-ray photoelectron spectroscopy (XPS) and optical spectroscopy. The Au(4f) XPS spectra illustrate substantial electron donation from the gold cores to the GS ligands in the Au:SG clusters. The optical absorption and photoluminescence spectra indicate that the electronic structures of the Au:SG clusters are well quantized: embryos of the sp band of the bulk gold evolve remarkably depending on the numbers of the gold atoms and GS ligands. The comparison of these spectral data with those of sodium Au(I) thiomalate and 1.8-nm Au:SG nanocrystals (NCs) reveals that the subnanometer-sized Au clusters thiolated constitute a distinct class of binary system which lies between the Au(I)-thiolate complexes and thiolate-protected Au NCs.

#### Reference

1) Y. Negishi *et al.*, *J. Am. Chem. Soc.* **126**, 6518 (2004).

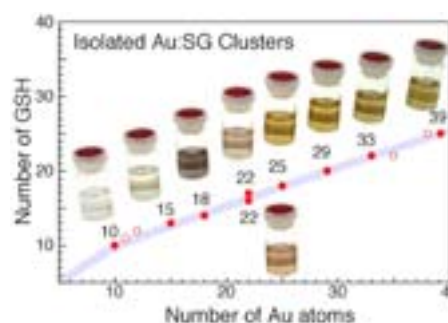


**Figure 1.** Chemical compositions of the Au:SG clusters isolated in the present study.

### IX-P-2 Large-Scale Synthesis of Thiolated Au<sub>25</sub> Clusters via Ligand Exchange Reactions of Phosphine-Stabilized Au<sub>11</sub> Clusters

SHICHIBU, Yukatsu<sup>1</sup>; NEGISHI, Yuichi;  
TSUKUDA, Tatsuya; TERANISHI, Toshiharu<sup>2</sup>  
(<sup>1</sup>JAIST; <sup>2</sup>Univ. Tsukuba)

[*J. Am. Chem. Soc.* **127**, 13464–13465 (2005)]

Phosphine-stabilized Au<sub>11</sub> clusters in chloroform were reacted with glutathione (GSH) in water under a nitrogen atmosphere. The resulting Au:SG clusters exhibit an optical absorption spectrum similar to that of Au<sub>25</sub>(SG)<sub>18</sub>, which was isolated as the major product from chemically prepared Au:SG clusters.<sup>1)</sup> Rigorous characterization by optical spectroscopy, electrospray ionization mass spectrometry, and polyacrylamide gel electrophoresis confirms that the Au<sub>25</sub>(SG)<sub>18</sub> clusters were selectively obtained on the sub-100-mg scale by ligand exchange reaction under aerobic conditions. The ligand exchange strategy offers a practical and convenient method of synthesizing thiolated Au<sub>25</sub> clusters on a large scale.

#### Reference

1) Y. Negishi *et al.*, *J. Am. Chem. Soc.* **127**, 5261 (2005).



**Figure 1.** Large-scale synthesis of the Au<sub>25</sub>(SG)<sub>18</sub> clusters via ligand exchange reactions.

### IX-P-3 Subnanometer-Sized Gold Clusters with Dual Molecular Receptors: Synthesis and Assembly in One-Dimensional Arrangements

NEGISHI, Yuichi; TSUNOYAMA, Hironori;  
YANAGIMOTO, Yasushi<sup>1</sup>; TSUKUDA, Tatsuya  
(<sup>1</sup>Okayama Univ.)

[*Chem. Lett.* **34**, 1638–1639 (2005)]

The gold (Au:S- $\beta$ -CD) clusters modified by thiolated  $\beta$ -cyclodextrin (HS- $\beta$ -CD) were prepared by reduction of AuCl<sub>4</sub><sup>-</sup> with NaBH<sub>4</sub> in DMSO solution: the concentration ratio, [HS- $\beta$ -CD]/[AuCl<sub>4</sub><sup>-</sup>], was fixed at 1. Interestingly, the core size distribution of the Au:S- $\beta$ -CD clusters determined by TEM measurements exhibits bimodal core-size distribution centered at *ca.* 1.1 and 2.4 nm. These two components were successfully separated by using polyacrylamide gel electrophoresis (PAGE). The low-mobility clusters contain the Au cores with the average diameter of 2.3 $\pm$ 0.4 nm whose optical absorption spectrum exhibits the surface plasmon band peaked at *ca.* 520 nm. In contrast, the Au clusters with the sizes of  $\sim$ 1 nm are barely discernible in the TEM image of the high-mobility clusters (**Au-1**). The optical spectroscopy and the thermogravimetric measurement suggest that fraction **Au-1** is composed of the Au<sub>12–15</sub> cores protected by two  $\beta$ -CD ligands. Since the diameter of the circle made by seven sulfurs of the S- $\beta$ -CD is comparable to the Au core size, this result inevitably implies that two S- $\beta$ -CD ligands are attached to the Au core so that the hydrophobic cavities are pointed toward the opposite side. This structural hypothesis was confirmed by the formation of one-dimensional assemblies of **Au-1** through binding interaction with ferrocene dimers (see structure in Figure 1). By use of tailor-made molecules as linkers, the **Au-1** clusters may be assembled in well-ordered arrangements with desired symmetry and interparticle distance.

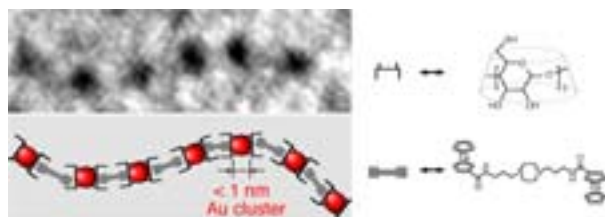


**Figure 1.** One-dimensional arrangements of **Au-1** formed by host-guest interaction with ferrocene dimers.

### IX-P-4 Size-Specific Catalytic Activity of Polymer-Stabilized Gold Nanoclusters for Aerobic Alcohol Oxidation in Water

TSUNOYAMA, Hironori; SAKURAI, Hidehiro;  
NEGISHI, Yuichi; TSUKUDA, Tatsuya<sup>1</sup>  
(<sup>1</sup>IMS, CREST)

[*J. Am. Chem. Soc.* **127**, 9374–9375 (2005)]

Gold nanoclusters ( $\phi$  = 1.3 nm) stabilized by poly(*N*-vinyl-2-pyrrolidone) (Au:PVP NCs) readily oxidize benzylic alcohols to the corresponding aldehydes and/or

carboxylic acids under ambient temperature in water. Kinetic measurement revealed that smaller Au:PVP NCs exhibit higher catalytic activity than larger (9.5 nm) homologues and, more surprisingly, than Pd:PVP NCs of comparable size (1.5 and 2.2 nm). On the basis of the marked difference in the kinetic isotope effect and activation energy between Au:PVP and Pd:PVP NCs, a reaction mechanism for alcohol oxidation catalyzed by Au:PVP NCs is proposed in which a superoxo-like molecular oxygen species adsorbed on the surface of the small Au NCs abstracts a hydrogen atom from the alkoxide.

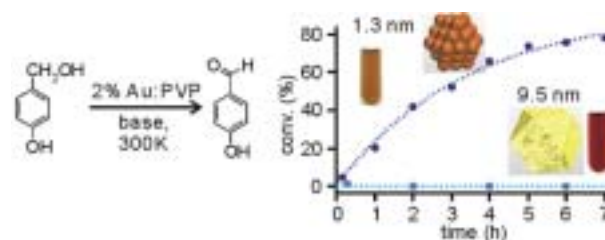


**Figure 1.** Time-course of conversion of *p*-hydroxyl benzyl alcohol by Au:PVP NCs ( $\phi$  = 1.3 and 9.5 nm).

### IX-P-5 Fabrication of Two dimensional Arrays of Size-Selected Gold Clusters

TSUNOYAMA, Hironori; NEGISHI, Yuichi;  
TSUKUDA, Tatsuya<sup>1</sup>  
(<sup>1</sup>IMS, CREST)

Alkanethiolate-protected gold (Au:SR) clusters of the size range of 1 ~ 5 nm were prepared by a ligand exchange of polymer-stabilized gold clusters (Au:PVP)<sup>1</sup> dispersed in water and subsequent heat treatment.<sup>2</sup> The Au:SR clusters thus obtained were size selected by using gel permeation chromatography (GPC).<sup>3</sup> The mass spectrometric characterization of the fractionated samples has revealed that the magic-numbered gold clusters with core masses of 8 kDa (1.1 nm), 14 kDa (1.3 nm), 22 kDa (1.5 nm), and 28 kDa (1.7 nm)<sup>4</sup> can be isolated by the GPC in a recycled operation. As for the Au:SR clusters of > 2 nm, the GPC separation yielded the sized selected clusters with a resolution of one atomic shell (0.5 nm in diameter). Two-dimensional arrays of the size-selected Au:SR clusters were fabricated by Langmuir-Brodgett technique. The structures of the films transferred to the amorphous carbon and other substrates (graphite and titania) were characterized by TEM, AFM, and SEM. Fabrication of model catalytic systems by using the cluster film thus prepared is now underway in collaboration with the groups of Profs. Al-Shamery (Oldenburg Univ.) and Matsumoto (IMS).

#### References

- 1) H. Tsunoyama *et al.*, *Langmuir* **20**, 11293 (2004).
- 2) T. Shimizu *et al.*, *J. Phys. Chem. B* **107**, 2719 (2003).
- 3) H. Murayama *et al.*, *J. Phys. Chem. B* **108**, 3496 (2004).
- 4) T. G. Schaaff *et al.*, *J. Phys. Chem. B* **101**, 7885 (1997).

## IX-Q Structural Analyses of Biological Macromolecules by Ultra-High Field NMR Spectroscopy

Our research seeks the underlying molecular basis for the function of biological macromolecules. In particular, we are interested in the function of molecular machines that work in the cellular processes involving protein folding, transport and degradation, and of glycoproteins playing important roles in the humoral and cellular immune systems. By use of ultra-high field NMR spectroscopy, we aim to elucidate the three-dimensional structure, dynamics, and interactions of proteins and glycoconjugates at the atomic level. A knowledge gained in this project will provide the structural basis for the rational design of drugs and biomolecular engineering that contribute towards a detailed understanding of biological systems.

### IX-Q-1 Ultra-High Field NMR Study of Carbohydrate-Protein Interactions

KAMIYA, Yukiko<sup>1</sup>; YAMAGUCHI, Yoshiki<sup>2</sup>;  
SASAKAWA, Hiroaki<sup>1</sup>; KATO, Koichi<sup>1</sup>  
(<sup>1</sup>IMS and Nagoya City Univ.; <sup>2</sup>Nagoya City Univ.)

NMR analyses of glycans have been hampered by spectral overlap and low sensitivity. It is obviously advantageous to measure NMR spectra of these molecules at an ultra-high magnetic field because of high resolution and high sensitivity. We demonstrate that the 920 MHz NMR spectra provide us with atomic information on complicated glycoconjugates.

The vesicular integral protein of 36 kDa (VIP36) is an intracellular animal lectin, which act as a putative cargo receptor recycling between the Golgi and the endoplasmic reticulum. Although VIP36 has been reported to recognize glycoproteins carrying high mannose-type oligosaccharides, very little has been known about structural aspects of the sugar-binding modes of this cargo receptor. We have therefore analyzed the interactions between a recombinant carbohydrate recognition domain of VIP36 (VIP36-CRD) and chemically synthesized oligosaccharides by use of nuclear magnetic resonance spectroscopy.

Figure 1a shows the anomeric regions of the 500 MHz <sup>1</sup>H NMR spectra of Man<sub>9</sub>GlcNAc<sub>2</sub>. The signals derived from Man-D1, Man-D2 and Man-D3 are severely degenerated. In contrast, these peaks are perfectly separated in the 920 MHz NMR spectrum (Figure 1b).

The one-dimensional <sup>1</sup>H NMR spectra of Man<sub>9</sub>GlcNAc<sub>2</sub> titrated with VIP36-CRD were observed for identification of sugar residues involved in binding to this lectin domain. Upon titration with VIP36-CRD, selective line broadening was observed for the signals originating from the mannose residues at positions 4, C, and D1, which correspond to the D1 arm of the Man<sub>9</sub>GlcNAc<sub>2</sub> (Figure 1c,d). On the basis of these data, we conclude that VIP36-CRD interacts predominantly with the D1 arm of high-mannose oligosaccharides.

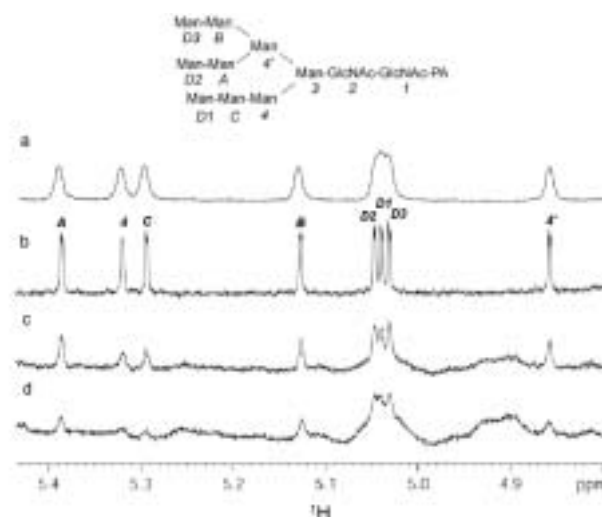


**Figure 1.** <sup>1</sup>H NMR spectra of oligosaccharide, Man<sub>9</sub>GlcNAc<sub>2</sub> (anomeric region). These spectra were recorded at the <sup>1</sup>H frequency of 500 MHz(a) and 920 MHz(b-d) in the absence (a, b) and presence of 0.2 equiv.(c) and 0.5 equiv.(d) of VIP36-CRD.

### IX-Q-2 Ultra-High Field NMR Study of Glycoproteins

NAGANO, Mayumi<sup>1</sup>; YAMAGUCHI, Yoshiki<sup>2</sup>;  
SASAKAWA, Hiroaki<sup>1</sup>; KATO, Koichi<sup>1</sup>  
(<sup>1</sup>IMS and Nagoya City Univ.; <sup>2</sup>Nagoya City Univ.)

Many of the proteins in the living systems express carbohydrate moieties. Although the biological importance of oligosaccharides covalently linked to proteins has been widely recognized, little is known about their specific roles from the structural aspect. This deficiency in our knowledge is largely due to the lack of an appropriate methodology to deal with glycoproteins as targets of structural biology. The carbohydrate moieties of glycoproteins generally exhibit microheterogeneities and possess a significant degree of freedom in internal motion, which hampers crystallization or interpretation of electron density. NMR spectroscopy can potentially provide us with information on structure and dynamics of glycoproteins in solution. However, there are few reports of structural determination of glycoproteins by NMR spectroscopy. In this situation, we have been developing NMR techniques for structural analyses at atomic resolution of glycoproteins in solution. In this methodology, the glycans and/or polypeptides of glyco-

proteins are uniformly or selectively labeled with stable isotopes ( $^{13}\text{C}$ ,  $^{15}\text{N}$ , and  $^2\text{H}$ ) by metabolic or enzymatic manners. We demonstrate our strategy using the Fc portion of immunoglobulin G (IgG) as a model system. A series of double and triple resonance experiments were performed for the uniformly  $^{13}\text{C}/^{15}\text{N}$ -labeled IgG-Fc. Figure 1 shows the 2D HSQC spectrum of IgG-Fc recorded on a 920 MHz NMR spectrometer. These spectra enabled us to assign the signals originating from the polypeptide backbone and the carbohydrate moieties. The NMR spectral data provide us with the basis for elucidation of structure and dynamics of the carbohydrate moieties as well as the polypeptide chains of the Fc glycoprotein in solution.

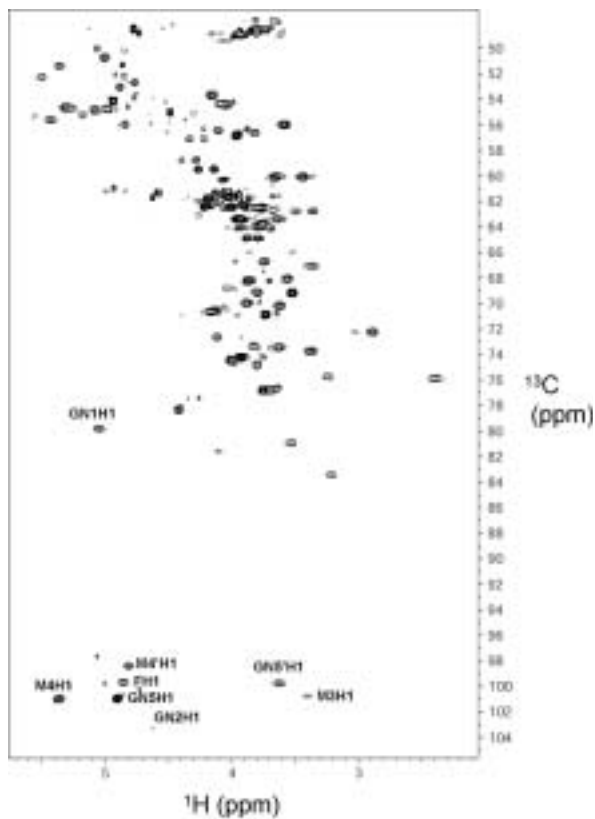


**Figure 1.**  $^1\text{H}$ - $^{13}\text{C}$  HSQC spectrum of the carbohydrate moieties of isotopically labeled IgG-Fc. The assignments of anomeric peaks are indicated in the spectrum.

## IX-R Electronic Structure and Collision Dynamics of Atoms and Molecules Studied by Electron Impact at Large Momentum Transfer

Binary ( $e,2e$ ) or electron momentum spectroscopy (EMS) is a high-energy electron-impact ionization experiment at large momentum transfer. The method involves coincident detection of the two outgoing electrons, allowing one to measure electron momentum densities for individual transitions or to look at molecular orbitals in momentum space. For molecular targets, however, EMS has long been plagued by the fact that the conventional ( $e,2e$ ) experiments measure averages over all orientations of gaseous targets; the spherical averaging results in enormous loss of versatile information on the target electronic structure, anisotropy of the target wavefunction in particular. To overcome the historical experimental difficulty, we have proposed the ( $e,2e+M$ ) method based on axial recoil fragmentation of the residual molecular ion and molecular frame ( $e,2e$ ) cross sections have been successfully measured for the first time. Further attempts along this line are now in progress, opening the door for detailed studies of bound electronic wavefunctions of molecules as well as of stereodynamics of electron-molecule collisions.

### IX-R-1 Development and Use of a Multichannel ( $e,2e$ ) Spectrometer for Electron Momentum Densities of Molecules

TAKAHASHI, Masahiko<sup>1</sup>; UDAGAWA, Yasuo<sup>1</sup>  
(<sup>1</sup>IMS and Tohoku Univ.)

[*J. Phys. Chem. Solids* **65**, 2055–2059 (2004)]

We have developed an ( $e,2e$ ) spectrometer with the introduction of modern multiparameter techniques. In particular, the high sensitivity achieved by simultaneous detection in energy and momentum is remarkable, opening up the possibilities of more precise and more advanced studies on the electronic structure of atoms and molecules. To illustrate some of the features, an overview of our recent results is presented. Highlights are applications to collision dynamics of H<sub>2</sub> and development of a method for a complete three-dimensional mapping of electron momentum densities in gaseous molecules. Both of these studies are based on the high sensitivity of the spectrometer.

### IX-R-2 Observation of Molecular Frame ( $e,2e$ ) Cross Section Using an Electron-Electron-Fragment Ion Triple Coincidence Apparatus

TAKAHASHI, Masahiko<sup>1</sup>; WATANABE, Noboru<sup>1</sup>; KHAJURIA, Yugal<sup>2</sup>; NAKAYAMA, Kazuya<sup>3</sup>; UDAGAWA, Yasuo<sup>1</sup>; ELAND, John H. D.<sup>4</sup>  
(<sup>1</sup>IMS and Tohoku Univ.; <sup>2</sup>IMS and IIT Madras; <sup>3</sup>Tohoku Univ.; <sup>4</sup>IMS and Oxford Univ.)

[*J. Electron Spectrosc. Relat. Phenom.* **141**, 83–93 (2004)]

An apparatus for electron-electron-fragment ion triple coincidence experiments has been developed to examine binary ( $e,2e$ ) scattering reaction in the molecular frame. In the axial recoil limit of fragmentation of the residual ion, measurements of vector correlations among the three charged particles are equivalent to ( $e,2e$ ) experiments with fixed-in-space molecules. Details and performance of the apparatus are reported, together with preliminary result of collision dynamics

study on ionization-excitation processes of fixed-in-space H<sub>2</sub> molecules. We believe that this is the first observation of molecular frame ( $e,2e$ ) cross sections.

### IX-R-3 ( $e,3e$ ) Collisions on Mg in the Impulsive Regime Studied by Second Born Approximation

WATANABE, Noboru<sup>1</sup>; COOPER, John W.<sup>2</sup>; VAN BOEYEN, Roger W.<sup>3</sup>; DOERING, John P.<sup>3</sup>; MOORE, John H.<sup>2</sup>; COPLAN, Michael A.<sup>2</sup>  
(<sup>1</sup>IMS and Tohoku Univ.; <sup>2</sup>Univ. Maryland; <sup>3</sup>Johns Hopkins Univ.)

[*J. Phys. B: At., Mol. Opt. Phys.* **37**, 4551–4560 (2004)]

Five-fold differential cross sections for electron-impact double ionization of the 3s electrons of magnesium have been calculated in the second Born approximation in the impulsive regime. Comparing these results with calculations carried out in the first Born approximation demonstrates the dominant contribution of the second Born term. The second Born calculation shows that contribution of the two-step 2 (TS2) process becomes large under the condition where sequential binary collisions on the Bethe ridge can occur. The effect of electron correlation in the initial target state is also examined by using a configuration interaction wavefunction.

### IX-R-4 Electron Momentum Spectroscopy of Valence Satellites of Neon

WATANABE, Noboru<sup>1</sup>; KHAJURIA, Yugal<sup>2</sup>; TAKAHASHI, Masahiko<sup>1</sup>; UDAGAWA, Yasuo<sup>1</sup>  
(<sup>1</sup>IMS and Tohoku Univ.; <sup>2</sup>IMS and IIT Madras)

[*J. Electron Spectrosc. Relat. Phenom.* **142**, 325–334 (2005)]

Electron momentum spectroscopy (EMS) study of the neon valence satellites is reported. The experiments were performed at impact energies of 1250, 1450 and 1670 eV using a multichannel spectrometer that features high sensitivity. Binding energy spectra up to 100 eV

and momentum profiles for the  $2p^{-1}$  and  $2s^{-1}$  primary transitions as well as the satellites are presented. The results are used to examine impact energy dependence of the relative intensities and shapes of the satellite momentum profiles. The results are also used to determine symmetries and spectroscopic factors of the satellites, and are compared with the previous experiments by EMS and photoelectron spectroscopy and sophisticated theoretical calculations. The present study has largely resolved controversies in the previous studies.

#### IX-R-5 Theoretical Fine Spectroscopy with Symmetry-Adapted-Cluster Configuration-Interaction Method: Outer- and Inner-Valence Ionization Spectra of Furan, Pyrrole, and Thiophene

EHARA, Masahiro<sup>1</sup>; OHTSUKA, Yuhki<sup>1</sup>;  
NAKATSUJI, Hiroshi<sup>1</sup>; TAKAHASHI, Masahiko<sup>2</sup>;  
UDAGAWA, Yasuo<sup>2</sup>

(<sup>1</sup>Kyoto Univ.; <sup>2</sup>IMS and Tohoku Univ.)

[*J. Chem. Phys.* **122**, 234319 (10 pages) (2005)]

Theoretical fine spectroscopy has been performed for the valence ionization spectra of furan, pyrrole, and thiophene with the symmetry-adapted-cluster configuration-interaction general-*R* method. The present method described that the  $\pi^1$  state interacts with the  $\pi_3^{-2}\pi^*$ ,  $\pi_2^{-2}\pi^*$ , and  $\pi_2^{-1}\pi_3^{-1}\pi^*$  shake-up states providing the split peaks and the outer-valence satellites, both of which are in agreement with the experiments. The intensity distributions were analyzed in detail for the inner-valence-region. In particular, for furan, theoretical intensities were successfully compared with the intensity measured by the electron momentum spectroscopy. The interactions of the  $3b_2$  and  $5a_1$  states with the shake-up states were remarkable for furan and pyrrole, while the  $4b_2$  state of thiophene had relatively large intensity.

#### IX-R-6 Observation of a Molecular Frame (*e,2e*) Cross Section: An (*e,2e+M*) Triple Coincidence Study on H<sub>2</sub>

TAKAHASHI, Masahiko<sup>1</sup>; WATANABE, Noboru<sup>1</sup>;  
KHAJURIA, Yugal<sup>2</sup>; UDAGAWA, Yasuo<sup>1</sup>; ELAND,  
John H. D.<sup>3</sup>

(<sup>1</sup>IMS and Tohoku Univ.; <sup>2</sup>IMS and IIT Madras; <sup>3</sup>IMS and Oxford Univ.)

[*Phys. Rev. Lett.* **94**, 213202 (4 pages) (2005)]

We report the first experimental results showing transition-specific anisotropy of molecular frame (*e,2e*) cross sections. Vector correlations between the two outgoing electrons and the fragment ion have been measured for specific ionization-excitation processes of H<sub>2</sub>. The results enable us to obtain molecular frame (*e,2e*) cross sections for transitions to the  $2s\sigma_g$  and  $2p\sigma_u$  excited states of H<sub>2</sub><sup>+</sup>, thereby making stereodynamics of the electron-molecule collisions directly visible.

#### IX-R-7 (*e,2e*) and (*e,3-1e*) Studies on Double Processes of He at Large Momentum Transfer

WATANABE, Noboru<sup>1</sup>; KHAJURIA, Yugal<sup>2</sup>;  
TAKAHASHI, Masahiko<sup>1</sup>; UDAGAWA, Yasuo<sup>1</sup>;  
VINITSKY, Pavel S.<sup>3</sup>; POPOV, Yuri V.<sup>3</sup>;  
CHULUUNBAATAR, Ochbadrakh<sup>4</sup>; KOZAKOV,  
Konstantin A.<sup>3</sup>

(<sup>1</sup>IMS and Tohoku Univ.; <sup>2</sup>IMS and IIT Madras;  
<sup>3</sup>Moscow State Univ.; <sup>4</sup>JINR)

[*Phys. Rev. A* **72**, 32705 (11 pages) (2005)]

The double processes of He in electron-impact ionization, single-ionization with simultaneous excitation and double-ionization, have been studied at large momentum transfer using an energy- and momentum-dispersive binary (*e,2e*) spectrometer. The experiment has been performed at an impact energy of 2080 eV in the symmetric noncoplanar geometry. In this way we have achieved a large momentum transfer of 9 a.u., a value that has never been realized so far for the study on double-ionization. The measured (*e,2e*) and (*e,3-1e*) cross sections for transitions to the  $n = 2$  excited state of He<sup>+</sup> and to doubly ionized He<sup>2+</sup> are presented as normalized intensities relative to that to the  $n = 1$  ground state of He<sup>+</sup>. The results are compared with first-order plane-wave impulse approximation (PWIA) calculations using various He ground-state wavefunctions. It is shown that shapes of the momentum-dependent (*e,2e*) and (*e,3-1e*) cross sections are well reproduced by the PWIA calculations only when highly correlated wavefunctions are employed. However, noticeable discrepancies between experiment and theory remain in magnitude for both the double processes, suggesting importance of higher-order effects under the experimental conditions examined as well as of acquiring more complete knowledge of electron correlation in the target.

#### IX-R-8 Electron Momentum Spectroscopy of the HOMO of Acetone

CHO, Tegyon<sup>1</sup>; TAKAHASHI, Masahiko<sup>2</sup>;  
UDAGAWA, Yasuo<sup>2</sup>

(<sup>1</sup>Tohoku Univ.; <sup>2</sup>IMS and Tohoku Univ.)

[*J. Photochem. Photobiol.* in press]

Electron momentum profiles of the HOMO of acetone have been measured under experimental conditions where a use of the plane-wave impulse approximation is justified. A double peak is observed in the experimental profile and it was found that calculated profiles by the use of the standard basis set always underestimate the magnitude of the low momentum peak. Possible origins of the discrepancies between the calculated and measured profiles are examined, leading to an improved agreement by modifying the exponents of diffuse functions employed.

**IX-R-9 ( $e,3-1e$ ) Reactions at Large Momentum Transfer: The Plane-Wave Second Born Approximation**

VINITSKY, Pavel S.<sup>1</sup>; POPOV, Yuri V.<sup>1</sup>;  
KOZAKOV, Konstantin A.<sup>1</sup>; WATANABE,  
Noboru<sup>2</sup>; TAKAHASHI, Masahiko<sup>2</sup>  
(<sup>1</sup>Moscow State Univ.; <sup>2</sup>IMS and Tohoku Univ.)

[*Phys. Rev. A* to be submitted]

We consider theoretically symmetric ( $e,3-1e$ ) reactions of He atom at large momentum transfer. For evaluating the corresponding four-fold differential cross sections, a theory based on the re-normalized plane-wave second Born approximation (SBA) is developed. The numerical SBA calculations for both coplanar and non-coplanar symmetric geometries are performed and compared with experiments.

**IX-R-10 Binary ( $e,2e$ ) Study on Xe: Momentum Profile for the 4d Orbital Revisited**

KHAJURIA, Yugal<sup>1</sup>; TAKAHASHI, Masahiko<sup>2</sup>;  
WATANABE, Noboru<sup>2</sup>; UDAGAWA, Yasuo<sup>2</sup>;  
YOSHINO, Tae<sup>3</sup>; SAKAI, Yasuhiro<sup>3</sup>;  
MUKOYAMA, Takeshi<sup>4</sup>  
(<sup>1</sup>IMS and IIT Madras; <sup>2</sup>IMS and Tohoku Univ.; <sup>3</sup>Toho Univ.; <sup>4</sup>Kansai Gaidai Univ.)

[*J. Phys. B: At. Mol. Opt. Phys.* to be submitted]

Binary ( $e,2e$ ) cross sections have been measured for Xe using an energy- and momentum-dispersive multi-channel spectrometer at impact energy of 2055 eV. Assuming that the Xe 5p ionization process can be described by the distorted-wave Born approximation (DWBA), the experimental momentum profile for the 4d orbital was placed on an absolute scale. The absolute-scale Xe 4d experiment has been compared with DWBA calculations using the Hartree-Fock and Dirac-Fock wavefunctions, in order to exploit relativistic effects in both shape and intensity of momentum profile. Although DWBA/DF has been found to give better description than DWBA/HF, noticeable discrepancies between experiment and theory still remain.

**IX-R-11 Binary ( $e,2e$ ) Study on Inner Shell Orbitals of Ar and Xe**

MIYAKE, Yusuke<sup>1</sup>; SHIBUYA, Masahiro<sup>1</sup>;  
TAKAHASHI, Masahiko<sup>2</sup>; WATANABE, Noboru<sup>2</sup>;

UDAGAWA, Yasuo<sup>2</sup>; SAKAI, Yasuhiro<sup>3</sup>;  
MUKOYAMA, Takeshi<sup>4</sup>  
(<sup>1</sup>Tohoku Univ.; <sup>2</sup>IMS and Tohoku Univ.; <sup>3</sup>Toho Univ.;  
<sup>4</sup>Kansai Gaidai Univ.)

[*J. Phys. B: At. Mol. Opt. Phys.* to be submitted]

Binary ( $e,2e$ ) experiments were performed on Xe 4p, 4s and Ar 2p, 2s orbitals. The results are compared with distorted-wave Born approximation calculations using the Hartree-Fock and Dirac-Fock wavefunctions, in order to exploit relativistic effects in momentum profile. Furthermore, for Xe the experiments have revealed a broad band at around 100 eV, which has not been found by photoelectron spectroscopy. The band has been assigned as giant resonance of Xe 4d in the sequential two collisions of the projectile with the target electrons.

**IX-R-12 Construction of a New ( $e,2e+M$ ) Apparatus for Complete Imaging of Molecular Orbitals**

TAKAHASHI, Masahiko<sup>1</sup>; WATANABE, Noboru<sup>1</sup>;  
SHIBUYA, Masahiro<sup>2</sup>; MIYAKE, Yusuke<sup>2</sup>;  
UDAGAWA, Yasuo<sup>1</sup>; MIZUTANI, Nobuo; SUZUI,  
Mitsukazu; MIURA, Kazuhiro<sup>2</sup>; YANAGIDA,  
Satomi<sup>2</sup>; MINEGISHI, Kouji<sup>2</sup>; JAGUTZKI,  
Ottmar<sup>3</sup>; DÖRNER, Reinhard<sup>3</sup>  
(<sup>1</sup>IMS and Tohoku Univ.; <sup>2</sup>Tohoku Univ.; <sup>3</sup>Univ.  
Frankfurt)

We have constructed a new electron-electron-fragment ion triple coincidence apparatus for complete imaging of molecular orbitals. The major sections of the apparatus are a chamber equipped with a 2300 L/s turbo molecular pump, an electron gun, a spherical analyzer followed by a hexagonal delay-line position-sensitive detector which covers the full  $2\pi$  azimuth of the two outgoing electrons emerging at the scattering angle of  $45^\circ$ , a velocity imaging system to detect all of parent and fragment ions from the  $4\pi$  solid angle, and data gathering electronics. The electron gun and spherical analyzer have been developed at the machine shop of the Tohoku University, while the chamber and the data gathering electronics have been developed at the equipment development center of IMS. This project aims at fully extending our preliminary ( $e,2e+M$ ) studies [M. Takahashi *et al.*, *J. Phys. Chem. Solids* **65**, 2055 (2004); *J. Electron Spectrosc. Relat. Phenom.* **141**, 83 (2004); *Phys. Rev. Lett.* **94**, 213202 (2005)], which have made it possible to perform molecular frame ( $e,2e$ ) spectroscopy for the first time.

**IX-S Electronic Structure and Collision Dynamics of Atoms and Molecules Studied by Photon Impact**

The group takes another, photon-impact, approach to issues of electronic structure and collision dynamics, since photon-impact and electron-impact or photoelectric effects and Compton scattering are complementary to each other.

### IX-S-1 Inner-Shell Photoelectron Angular Distributions from Fixed-in-Space OCS Molecules

GOLOVIN, Alexander V.<sup>1,2</sup>; ADACHI, Junichi<sup>1,3,4</sup>; MOTOKI, Souhei<sup>1</sup>; TAKAHASHI, Masahiko<sup>5</sup>; YAGISHITA, Akira<sup>1,3</sup>

(<sup>1</sup>KEK-PF; <sup>2</sup>St. Petersburg State Univ.; <sup>3</sup>Univ. Tokyo; <sup>4</sup>IMS; <sup>5</sup>IMS and Tohoku Univ.)

[*J. Phys. B: At. Mol. Opt. Phys.* **38**, L63–L68 (2005)]

The photoelectron angular distributions (PADs) for the OCS O 1s, C 1s and S 2p<sub>1/2</sub>, 2p<sub>3/2</sub> ionization have been measured in the shape resonance region. The experimental results have been compared with multiple scattering X $\alpha$  calculations. It is found that the position of an ionized atom plays a significant role. For a central position (C 1s ionization) the PAD is relatively symmetric. In the case of S 2p and O 1s ionization, electrons are emitted highly preferentially in a solid cone directed from the molecular centre to the respective S or O atom. For the OCS O 1s ionization the S–C fragment plays a very effective role as a ‘scatterer’ in the shape resonance region nearly all intensity in PAD is concentrated in the lobe between  $\theta = 50^\circ$  and  $80^\circ$ , but not along the molecular axis.

### IX-S-2 Coincidence Velocity Imaging Apparatus for the Study of Angular Correlations between Photoelectrons and Photofragments

HOSAKA, Kouichi<sup>1</sup>; ADACHI, Junichi<sup>1,2,3</sup>; GOLOVIN, Alexander V.<sup>2,4</sup>; TAKAHASHI, Masahiko<sup>5</sup>; WATANABE, Noboru<sup>5</sup>; YAGISHITA, Akira<sup>1,2</sup>

(<sup>1</sup>Univ. Tokyo; <sup>2</sup>KEK-PF; <sup>3</sup>IMS; <sup>4</sup>St. Petersburg State Univ.; <sup>5</sup>IMS and Tohoku Univ.)

[*J. Electron Spectrosc. Relat. Phenom.* submitted]

A new apparatus of coincidence velocity mapping has been developed for studies on inner-shell photoionization dynamics of molecules. It achieves velocity imaging for electrons and ions simultaneously, and keeps the time focusing. To demonstrate the performance of the new apparatus, some examples, photoelectron angular distributions from Ne atoms and randomly oriented NO molecules, photoion angular distributions from CO molecules, and photoelectron angular distributions from fixed-in-space CO and NO molecules, are reported.

### IX-S-3 Non-Dipole Effects in the Angular Distribution of Photoelectrons from the K-Shell of N<sub>2</sub> Molecule

HOSAKA, Kouichi<sup>1</sup>; ADACHI, Junichi<sup>1,2,3</sup>; GOLOVIN, Alexander V.<sup>2,4</sup>; TAKAHASHI, Masahiko<sup>5</sup>; TERAMOTO, Takahiro<sup>1</sup>; WATANABE, Noboru<sup>5</sup>; YAGISHITA, Akira<sup>1,2</sup>; SEMENOV, Sergei K.<sup>6</sup>; CHEREPKOV, Nikolai A.<sup>6</sup>

(<sup>1</sup>Univ. Tokyo; <sup>2</sup>KEK-PF; <sup>3</sup>IMS; <sup>4</sup>St. Petersburg State

Univ.; <sup>5</sup>IMS and Tohoku Univ.; <sup>6</sup>State Univ. Aerospace Instrum.)

[*J. Phys. B: At. Mol. Opt. Phys.* submitted]

Measurements and calculations of contribution of the non-dipole terms in the angular distribution of photoelectrons from the K-shell of randomly oriented N<sub>2</sub> molecules are reported. The angular distributions have been measured in the plane containing the photon polarization and the photon momentum vectors of linearly polarized radiation. Calculations have been performed in the relaxed core Hartree-Fock approximation with a fractional charge, and many-electron correlations were taken into account in the random phase approximation. Both theory and experiment show that the non-dipole terms are rather small in the photon energy region from the ionization threshold of the K-shell up to about 70 eV above it. From the theory it follows that the non-dipole terms for the individual shells of 1 $\sigma_g$  and 1 $\sigma_u$  are considerably large, therefore measurements resolving the contributions of the 1 $\sigma_g$  and 1 $\sigma_u$  shells are desirable.

### IX-S-4 Direct Observation of a Symmetry Lowering in Core-Electron Ionization for Highly Symmetric Molecules

HOSAKA, Kouichi<sup>1</sup>; ADACHI, Junichi<sup>1,2,3</sup>; GOLOVIN, Alexander V.<sup>2,4</sup>; TAKAHASHI, Masahiko<sup>5</sup>; TERAMOTO, Takahiro<sup>1</sup>; WATANABE, Noboru<sup>5</sup>; YAGISHITA, Akira<sup>1,2</sup>

(<sup>1</sup>Univ. Tokyo; <sup>2</sup>KEK-PF; <sup>3</sup>IMS; <sup>4</sup>St. Petersburg State Univ.; <sup>5</sup>IMS and Tohoku Univ.)

The symmetry lowering occurs quite often in the ionization of a core electron of equivalent constituent-atoms for highly symmetric molecules since the core-hole states of those molecules are generally quasi-degenerate and therefore couple over non-totally symmetric vibrational modes. Such couplings, referred as quasi-Jahn-Teller couplings, have been clearly investigated for the most basic example of CO<sub>2</sub>; the relation between the symmetry lowering and core-hole localization has been proved. The symmetry lowering which removes the equivalence of two oxygen atoms causes a fundamental quantum mechanical question; is it possible to decide whether the core hole is localized on the right oxygen atom or on the left? Here we report the direct observation of the symmetry lowering of the CO<sub>2</sub> induced by O1s photoionization.

## IX-T Study of Electronic Structure of Organic Thin Film and Organic/Inorganic Interface

Organic semiconductors have attracted much interest due to their highly potential, flexibility, electronic and optical properties, and their considerable promise in molecular device technologies. To clarify the electronic properties at the organic/organic and organic/metal interface, various characterization techniques such as high-resolution ultraviolet photoemission spectroscopy (UPS) and near-edge x-ray absorption fine structure (NEXAFS) have been performed for organic thin film systems, because origin of the energy position, band shape and band width of UPS spectra are keys to understand the interface properties such as the energy level alignment at the interface, intermolecular or molecule-substrate interactions, and carrier transfer/transport process. Especially, vibronic coupling and lifetime of a hole created in the highest occupied molecular orbital (HOMO) state in the organic thin film play a crucial role in the hole transport through the film and the electron injection from an electrode to the ionized molecule. The HOMO band in UPS spectra in principle involves such information about the hole, and thus offers a variety of key information that is necessary to unravel fundamental mechanism in carrier dynamics in organic devices.

### IX-T-1 Deep Insight into a Valence Hole in Organic Semiconductors: High-Resolution Ultraviolet Photoemission Study

**KERA, Satoshi; UENO, Nobuo**<sup>1</sup>  
(<sup>1</sup>Chiba Univ.)

[*IPAP Conf. Ser.* **6**, 51–56 (2005)]

We have succeeded to observe a very sharp highest occupied molecular orbital (HOMO) band for oriented thin films of various phthalocyanines prepared on graphite *via* high-resolution ultraviolet photoelectron spectroscopy. Hole-vibration couplings can be resolved even for films of large  $\pi$ -conjugated molecules. The fine structure would give us lots information on “hidden” properties in organic-based devices, such as molecular-vibration related carrier dynamics, intermolecular interaction, and molecule-substrate interaction. Moreover, it was found that the observed binding energy position is much affected by inhomogeneity of the film with different molecular orientations, leading to a broadening of the HOMO bandwidth.

### IX-T-2 UPS Fine Structures of Highest Occupied Band in Vanadyl-Phthalocyanine Ultrathin Film

**FUKAGAWA, Hirohiko**<sup>1</sup>; **YAMANE, Hiroyuki**<sup>1</sup>;  
**KERA, Satoshi; OKUDAIRA, K. Koji**<sup>1</sup>; **UENO, Nobuo**<sup>1</sup>  
(<sup>1</sup>Chiba Univ.)

[*J. Electron Spectrosc.* **144-147**, 475–478 (2005)]

Ultraviolet photoelectron spectra were measured for vanadyl phthalocyanine (VOPc) ultrathin films prepared on graphite to study effects of the molecular orientation and the electric dipole layer on the organic electronic states. VOPc has a permanent electric dipole perpendicular to the molecular plane, hence a well-defined electric dipole layer could be intentionally prepared by using the oriented monolayer. The observed binding-energy difference of the highest occupied molecular orbital (HOMO) bands between the oriented monolayer

and the double layer was found to agree with the vacuum level shift, leading to a conclusion that the molecular energy level with respect to the substrate Fermi level is changed when the molecule is in the electric dipole layer.

### IX-T-3 Fine Structure of the Highest Occupied Band in OTi-Phthalocyanine Monolayer

**YAMANE, Hiroyuki**<sup>1</sup>; **FUKAGAWA, Hirohiko**<sup>1</sup>;  
**HONDA, Hiroyuki**<sup>1</sup>; **KERA, Satoshi; OKUDAIRA, K. Koji**<sup>1</sup>; **UENO, Nobuo**<sup>1</sup>  
(<sup>1</sup>Chiba Univ.)

[*Synth. Met.* **152**, 297–300 (2005)]

Ultraviolet photoelectron spectra were measured for ultrathin films of OTi-phthalocyanine (OTiPc), which has an electric dipole perpendicular to the molecular plane, prepared on highly oriented pyrolytic graphite in order to study effects of the molecular orientation and the electric dipole layer on the organic electronic states. For the as-grown films, the observed highest occupied molecular orbital (HOMO) band consists of two prominent peaks that can be assigned to different molecular orientations. For the oriented monolayer obtained by annealing the as-grown film, we detected a very sharp HOMO band at 290 K. The binding-energy ( $E_B$ ) difference between the HOMO bands of the as-grown and annealed films was found to agree with the shift in the vacuum level. For the oriented monolayer, the observed sharp HOMO band involves at least four components that are ascribed to the coupling between the HOMO hole and the molecular vibration. Upon cooling the sample to 95 K, the HOMO bandwidth became sharper than that at 290 K. From the peak fitting using Voigt function, additional components are expected in the HOMO band at 95 K. Moreover, we detected the  $E_B$  shift in the HOMO band for the oriented monolayer upon cooling, which can be originated from decrease in the HOMO-hole screening due to the change in the film structure and/or the molecule-substrate interaction.

### IX-T-4 Hole/Vibration Coupling of the Highest Occupied Band in Pentacene Thin Film

**YAMANE, Hiroyuki<sup>1</sup>; NAGAMATSU, Shin-ichi<sup>1</sup>;  
FUKAGAWA, Hirohiko<sup>1</sup>; KERA, Satoshi;  
FRIEDLEIN, Rainer<sup>2</sup>; OKUDAIRA, K. Koji<sup>1</sup>;  
UENO, Nobuo<sup>1</sup>**  
(<sup>1</sup>Chiba Univ.; <sup>2</sup>Linköping Univ.)

[*Phys. Rev. B* **72**, 153412 (4 pages) (2005)]

The hole-vibration coupling of the highest occupied state in pentacene thin films on graphite is studied by high-resolution ultraviolet photoelectron spectroscopy. Vibration satellites in the film show a take-off-angle dependence, indicating that the Frank-Condon principle is not strictly satisfied in this system. They are more intense than in the gas phase and the vibrational energy in the film is slightly lower than that in the gas phase. This demonstrates that the reorganization energy in pentacene thin films is slightly larger than that estimated from the photoelectron spectrum of free pentacene molecules. Furthermore, it is pointed out that the electron hopping in the low-temperature film may occur in the femtosecond scale before the electronic polarization of the surrounding medium is completed.

#### **IX-T-5 Quantitative Analysis of Photoelectron Angular Distribution of a Single Domain Organic Monolayer Film: NTCDA on GeS(001)**

**KERA, Satoshi; TANAKA, Shinji<sup>1</sup>; YAMANE, Hiroyuki<sup>1</sup>; YOSHIMURA, Daisuke<sup>2</sup>; OKUDAIRA, K. Koji<sup>1</sup>; SEKI, Kazuhiko<sup>3</sup>; UENO, Nobuo<sup>1</sup>**  
(<sup>1</sup>Chiba Univ.; <sup>2</sup>IMS and Nagoya Univ.; <sup>3</sup>Nagoya Univ.)

[*Chem. Phys.* in press]

Angle-resolved photoelectron spectra were measured for a single-crystal monolayer film of naphthalene-1,4,5,8-tetracarboxylic dianhydride (NTCDA) prepared on a cleaved GeS(001) surface using synchrotron radiation. The observed photoelectron angular distributions were analyzed by a calculation using the single-scattering approximation combined with molecular orbital calculation. With the help of the low-energy electron diffraction pattern, the structure of the NTCDA monolayer on GeS(001) was estimated quantitatively.

#### **IX-T-6 UPS Study of VUV-Photodegradation of Polytetrafluoroethylene (PTFE) Ultrathin Film by Using Synchrotron Radiation**

**ONO, Masaki<sup>1</sup>; YAMANE, Hiroyuki<sup>1</sup>;  
FUKAGAWA, Hirohiko<sup>1</sup>; KERA, Satoshi;  
YOSHIMURA, Daisuke<sup>2</sup>; OKUDAIRA, K. Koji<sup>1</sup>;  
MORIKAWA, Eiji<sup>3</sup>; SEKI, Kazuhiko<sup>4</sup>; UENO, Nobuo<sup>1</sup>**  
(<sup>1</sup>Chiba Univ.; <sup>2</sup>IMS and Nagoya Univ.; <sup>3</sup>CAMD;  
<sup>4</sup>Nagoya Univ.)

[*Nucl. Instrum. Methods Phys. Res., Sect. B* **236**, 377–382 (2005)]

The VUV-photodegradation of polytetrafluoroethylene (PTFE) ultra-thin film was studied by ultraviolet photoelectron spectroscopy and quadrupole mass

spectrometry. These results were compared with the previous photodegradation studies of the polyvinylidene fluoride (PVDF) and polyethylene (PE). Generation of new peak,  $\pi$ -band originated from the C=C bond, was observed in the low binding energy region of the UPS spectra in both PVDF and PE during the photodegradation. In contrast, no new peak generation was observed in the UPS of the photodegraded PTFE. Mass spectrometry analysis also suggested that the C=C bond generation is not a major mechanism in the VUV photodegradation of PTFE.

#### **IX-T-7 Site-Specific Ion Desorption of Fluorinated Phthalocyanine Studied with Electron-Ion Coincidence Spectroscopy**

**OKUDAIRA, K. Koji<sup>1</sup>; WATANABE, Takahiro<sup>1</sup>;  
KERA, Satoshi; KOBAYASHI, Eiichi<sup>2</sup>; MASE, Kazuhiko<sup>2</sup>; UENO, Nobuo<sup>1</sup>**  
(<sup>1</sup>Chiba Univ.; <sup>2</sup>AIST)

[*J. Electron Spectrosc.* **144-147**, 464–464 (2005)]

Auger electron photo-ion coincidence (AEPICO) and Auger spectra of fluorinated copper phthalocyanine (F<sub>16</sub>CuPc) were observed to study the mechanism of the site-specific ion desorption. From the photon energy dependence of Auger electron spectra at fluorine (F) K-edge region, it is found that the spectator-Auger shift at  $h\nu = 691.4$  eV is about 2 eV. To estimate the contribution of spectator-Auger component to the Auger spectra, the difference Auger spectra were obtained by subtracting the Auger spectrum above F 1s ionization energy from observed Auger spectra. AEPICO yield spectra for F<sup>+</sup> at  $h\nu = 691.4$  eV gives a large intensity at  $E_{\text{kin}} = 650$  eV. The electron kinetic energy position of this intense F<sup>+</sup> AEPICO peak agrees with that of the difference Auger spectra, indicating that the most probable mechanism for F<sup>+</sup> ion desorption induced by the transition from F<sub>1s</sub> to  $\sigma(\text{C-F})^*$  is the spectator-Auger-stimulated ion desorption.

#### **IX-T-8 Polarized Near-Edge X-Ray-Absorption Fine Structure Spectroscopy of C<sub>60</sub>-Functionalized 11-Amino-1-Undecane Thiol Self-Assembled Monolayer: Molecular Orientation and Evidence for C<sub>60</sub> Aggregation**

**PATNAIK, Archita<sup>1</sup>; OKUDAIRA, K. Koji<sup>1</sup>; KERA, Satoshi; SETOYAMA, Hiroyuki<sup>1</sup>; MASE, Kazuhiko<sup>2</sup>; UENO, Nobuo<sup>1</sup>**  
(<sup>1</sup>Chiba Univ.; <sup>2</sup>AIST)

[*J. Chem. Phys.* **122**, 154703 (9 pages) (2005)]

Near-edge x-ray-absorption fine structure (NEXAFS) spectroscopy was adopted to probe the unoccupied electronic states of C<sub>60</sub> anchored onto an organized assembly of 11-amino-1-undecane thiol on Au(111). The polarization dependence of the intensity of  $\pi^*$  resonance associated with C<sub>60</sub>  $\pi$  network revealed the self-assembled monolayer (SAM) system to be oriented with an average molecular tilt angle of 57° with respect to the surface normal. Invoking the absence of solid-state band

dispersion effects and in comparison to solid C<sub>60</sub> and/or 1-ML C<sub>60</sub>/Au(111), the electronic structure of the resulting assembly was found dominated by spectral position shift and linewidth and intensity changes of the lowest unoccupied molecular orbital (LUMO), LUMO +1, and LUMO+2 orbitals. The latter implied hybridization between N *P<sub>z</sub>* of -NH<sub>2</sub> group of thiolate SAM and  $\pi$  levels of C<sub>60</sub>, resulting in a nucleophilic addition with a change in the symmetry of C<sub>60</sub> from *I<sub>h</sub>* to *C<sub>1</sub>* in the SAM. Occurrence of a new feature at 285.3 eV in the NEXAFS spectrum, assigned previously to  $\pi^*$  graphitic LUMO, signified the formation of aggregated clusters, (C<sub>60</sub>)<sub>*n*</sub> of C<sub>60</sub> monomer. Low tunneling current scanning tunneling microscopy confirmed them to be spherical and stable aggregates with *n* ~ 5.

# UVSOR Facility

## IX-U Development of the UVSOR Light Source

### IX-U-1 Successful Commissioning of New RF Cavity

MOCHIIHASHI, Akira; KATOH, Masahiro;  
HOSAKA, Masahito; YAMAZAKI, Jun-ichiro;  
HAYASHI, Kenji; TAKASHIMA, Yoshifumi<sup>1</sup>  
(<sup>1</sup>Nagoya Univ.)

We have built a new main RF accelerating cavity for the UVSOR-II electron storage ring. The new cavity can generate RF voltage of 150 kV without replacing the high power RF transmitter whose maximum output power is 20 kW. The cavity was installed in a short straight section in the spring 2005. The design RF voltage of 150 kV was soon achieved in the high-power test operation without electron beam. After the high power test operation, the test operation with electron beam was started. By carefully observing the pressure rise in the cavity, we have decided to start the user operation with a moderately high RF accelerating RF voltage of 100 kV, which is twice higher than before. After the vacuum is completely recovered, the operation with the design voltage of 150 kV will be started. These high values of the accelerating voltage have made the low emittance operation possible without reducing the

beam lifetime. Since May 2005, the UVSOR-II electron storage ring has been operated with a small emittance of 27 nm-rad for users.

### IX-U-2 Ion Trapping Phenomena at UVSOR-II

MOCHIIHASHI, Akira; KATOH, Masahiro;  
HOSAKA, Masahito; YAMAZAKI, Jun-ichiro;  
HAYASHI, Kenji; TAKASHIMA, Yoshifumi<sup>1</sup>;  
HORI, Yoichiro<sup>2</sup>  
(<sup>1</sup>Nagoya Univ.; <sup>2</sup>KEK)

We have observed the dependence of the vertical betatron tune on the vacuum condition on the UVSOR-II electron storage ring. We changed the vacuum condition artificially by turning off the vacuum pumps. The betatron tune was measured by RF-KO method. During the experiment, the storage ring was operated in multi-bunch filling mode, in which successive twelve RF buckets were filled with electrons and other four buckets were kept empty. This result strongly suggested that the non-linear electric field produced by the ions trapped by the electron beam caused the betatron tune shift. We have observed betatron tune shifts were consistent with the theoretical predictions.

## IX-V Researches by the Use of UVSOR

### IX-V-1 Development of Velocity Imaging Spectrometer for Observing Negative Fragment Ions

HIKOSAKA, Yasumasa; SHIGEMASA, Eiji

[*J. Electron Spectrosc. Relat. Phenom.* **148**, 5 (2005)]

A velocity imaging spectrometer has been developed to observe negative ions from molecular ion-pair dissociation. The imaging spectrometer furnishes with a pair of permanent magnets. The formed magnetic field effectively prevents the electrons' arrivals to the detector, without seriously affecting negative ions' flights. The performance of the imaging spectrometer is demonstrated in the observations of photoelectrons from O<sub>2</sub> and He, and O<sup>-</sup> from O<sub>2</sub>. Sample results on negative ion formation from O<sub>2</sub> and N<sub>2</sub>O, prove that the present imaging method provides useful information on the assignments of superexcited states and the dynamical properties of ion-pair dissociation.

### IX-V-2 Dynamics of Double Photoionization near the Ar 2p Threshold Investigated by Threshold Electron-Auger Electron Coincidence Spectroscopy

LABLANQUIE, Pascal<sup>1</sup>; SEINERMAN, Sergei<sup>2</sup>;  
PENENT, Francis<sup>3</sup>; AOTO, Tomohiro<sup>4</sup>;  
HIKOSAKA, Yasumasa; ITO, Kenji<sup>4</sup>  
(<sup>1</sup>LURE; <sup>2</sup>St. Petersburg State Maritime Tech. Univ.;  
<sup>3</sup>LCPMR; <sup>4</sup>KEK)

[*J. Phys. B* **38**, L9 (2005)]

Threshold electron–Auger electron coincidence spectroscopy measurements were carried out near the Ar 2p thresholds. Such a method allows us, for the first time, to observe the threshold electron yields associated with the selected final states of the Ar<sup>2+</sup> ion: 3p<sup>4</sup>(<sup>1</sup>D<sub>2</sub>), 3p<sup>4</sup>(<sup>1</sup>S<sub>0</sub>), 3p<sup>4</sup>(<sup>3</sup>P) resulting from the 2p hole Auger decay. All the spectra reveal strong PCI distortion. Comparison with calculations carried out in the framework of a quantum-mechanical PCI model allows us to clarify the mechanisms and the dynamics of threshold electron production. In the 3p<sup>4</sup>(<sup>1</sup>D<sub>2</sub>) and 3p<sup>4</sup>(<sup>1</sup>S<sub>0</sub>) channels, contribution to the threshold electron yield comes essentially from the PCI retardation of slow photoelectrons. In the 3p<sup>4</sup>(<sup>3</sup>P) final state channel, an additional process of valence multiplet decay of the 3p<sup>4</sup>(<sup>1</sup>D<sub>2</sub>)6d state plays a role at and below the L<sub>2</sub>, L<sub>3</sub> thresholds.

**IX-V-3 Origin of Threshold Electrons Produced in Decay of the Xe  $4d^{-1}np$  Resonance**

AOTO, Tomohiro<sup>1</sup>; HIKOSAKA, Yasumasa;  
HALL, Richard<sup>2</sup>; PENENT, Francis<sup>2</sup>;  
LABLANQUIE, Pascal<sup>3</sup>; ITO, Kenji<sup>1</sup>  
(<sup>1</sup>KEK; <sup>2</sup>DIAM; <sup>3</sup>LURE)

[*J. Electron Spectrosc. Relat. Phenom.* **142**, 319 (2005)]

Coincidence spectra of energetic electrons with threshold electrons were measured following photo-excitation of the Xe  $4d_{3/2,5/2} \rightarrow np$  resonances, in order to investigate the origin of threshold electrons, and the mechanism leading to formation of the Xe<sup>2+</sup>  $5p^{-2}$  and  $5s^{-1}5p^{-1}$  final states. A two-step decay process was observed in the production of Xe<sup>2+</sup>  $5p^{-2}(^1D)$  following decay of the  $7p$  resonance, where the intermediate state is Xe<sup>++</sup>  $5p^{-2}(^1S)8p$  that autoionizes emitting a pseudo-threshold electron. This process was confirmed in a time-of-flight analysis of the coincidence spectra of the energetic electrons with the threshold photoelectrons. It is suggested that a similar two-step process also contributes to the population of excited Xe<sup>2+</sup> states and is the main origin for the production of threshold electrons in decay of the  $4d^{-1} np$  resonances.

**IX-V-4 Coincidence Auger Spectroscopy**

PENENT, Francis<sup>1,2</sup>; LABLANQUIE, Pascal<sup>3</sup>;  
HALL, Richard<sup>2</sup>; PALAUDOUX, Jerome<sup>1</sup>; ITO,  
Kenji<sup>4</sup>; HIKOSAKA, Yasumasa; AOTO,  
Tomohiro<sup>4</sup>; ELAND, John H. D.<sup>5</sup>  
(<sup>1</sup>LCPMR; <sup>2</sup>DIAM; <sup>3</sup>LURE; <sup>4</sup>KEK; <sup>5</sup>PTCL)

[*J. Electron Spectrosc. Relat. Phenom.* **144-147**, 7  
(2005)]

Auger electron spectroscopy (AES) and photoelectron spectroscopy (PES) are (with X-ray emission spectroscopy, XES) powerful analytical tools for material science and gas phase studies. However, the interpretation of Auger spectra can be very difficult due to the number and complexity of the involved processes. A deeper analysis, that allows a better understanding of relaxation processes following inner shell ionization, is possible with coincidence Auger spectroscopy. This method gives a new insight into electron correlation and allows disentangling of complex Auger electron spectra. In this paper, we present some examples related to gas phase coincidence Auger electron spectroscopy using synchrotron radiation. The detection in coincidence of an Auger electron with a threshold photoelectron presents two main advantages which are good energy resolution and high coincidence count rates. This technique has also provided new results on double Auger decay processes. A further qualitative breakthrough has been made with the development of a new experimental setup based on a magnetic bottle time-of-flight electron spectrometer. This opens up the field of multi-electron coincidence spectroscopy and allows a most detailed analysis with characterization of all possible decay pathways following inner shell ionization.

**IX-V-5 Collision Dynamics of the Kr<sup>8+</sup> + N<sub>2</sub> System Studied by a Multi-Coincidence Technique**

KANEYASU, Tatsuo; AZUMA, Toshiyuki<sup>1</sup>;  
OKUNO, Kazuhiko<sup>1</sup>  
(<sup>1</sup>Tokyo Metropolitan Univ.)

[*J. Phys. B* **38**, 1341 (2005)]

We have developed a multi-coincidence technique to study MCI-molecule collisions. Using this technique, complicated reaction processes and collision dynamics in Kr<sup>8+</sup> + N<sub>2</sub> collisions have been successfully revealed in the energy region below 200 eV/u. The reaction processes in the single-, double-, triple- and quadruple-charge changing collisions are resolved and three low-energy collision phenomena, 'peak-shifting' of molecular ions, 'peak-splitting' and 'anisotropic fragmentation' of fragment ion pairs, are found in the time-of-flight spectra of target ions. By careful analysis of kinematics of all the products, it is concluded that the charge transfer in the Kr<sup>8+</sup> + N<sub>2</sub> collisions is dominated by multi-electron capture processes followed by electron emission and the collision dynamics is characterized by the transverse momentum transfer from the ion to the molecule and the appearance of the 'anisotropic fragmentation.'

**IX-V-6 Collision Dynamics of MCI-Molecule Systems Studied by Multi-Coincidence Technique**

KANEYASU, Tatsuo; AZUMA, Toshiyuki<sup>1</sup>;  
OKUNO, Kazuhiko<sup>1</sup>  
(<sup>1</sup>Tokyo Metropolitan Univ.)

[*Nucl. Instrum. Methods Phys. Res., Sect. B* **235**, 352  
(2005)]

Collision dynamics and reaction processes in charge transfer collisions of Kr<sup>8+</sup> + N<sub>2</sub> below 200 eV/u have been studied. We used a multi-coincidence technique which enables us to obtain kinematic information for both the fragment ions and the scattered projectile. The collision phenomena observed in the time-of-flight spectra of target ions are well clarified in consideration of the kinematics in colliding particles. We found an anisotropy in charge-unbalanced fragmentation channels at lower collision energy. The anisotropic behavior becomes significant not only with decreasing the collision energy but also with increasing the charge imbalance of the fragment ion-pair. The collision dynamics in the Kr<sup>8+</sup> + N<sub>2</sub> system is characterized by the transverse recoil momentum and the anisotropic fragmentation.

**IX-V-7 Optical Investigations of the Clathrate  $\alpha$ -Eu<sub>8</sub>Ga<sub>16</sub>Ge<sub>30</sub>**

SICHELSCHMIDT, Joerg<sup>1</sup>; VOEVODIN,  
Vladimir<sup>1</sup>; PACHECO, J.<sup>1</sup>; GRIN, Yuri<sup>1</sup>;  
STEGELICH, Frank<sup>1</sup>; NISHI, Tatsuhiko<sup>2</sup>; KIMURA,  
Shin-ichi

(<sup>1</sup>Max-Planck Inst.; <sup>2</sup>SOKENDAI)

[*Eur. Phys. J. B* **46**, 363–366 (2005)]

We performed measurements of the optical reflectivity in the energy range 0.007–30 eV on the clathrate-VIII type compound  $\alpha$ -Eu<sub>8</sub>Ga<sub>16-x</sub>Ge<sub>30-x</sub> in order to investigate its electronic band structure. The very low charge carrier concentration as well as ferromagnetic ordering of the divalent Eu ions below 10.5 K characterize the spectra at photon energies below ~0.4 eV in accordance with the results of band structure calculations. Disorder induced bound states have been identified to affect the optical conductivity at energies between 10 and 100 meV.

#### IX-V-8 Influence of Cage Distortions on the Electronic Structure and Optical Properties of Ba<sub>6</sub>Ge<sub>25</sub>

ZEREC, Ivica<sup>1</sup>; CARRILLO-CABRERA, Wilder<sup>1</sup>; VOEVODIN, Vladimir<sup>1</sup>; SICHELSCHMIDT, Joerg<sup>1</sup>; STEGLICH, Frank<sup>1</sup>; GRIN, Yuri<sup>1</sup>; YARESKO, Alexander<sup>1</sup>; KIMURA, Shin-ichi (<sup>1</sup>Max-Planck Inst.)

[*Phys. Rev. B* **72**, 045122 (7 pages) (2005)]

Measurements of the optical conductivity on Ba<sub>6</sub>Ge<sub>25</sub> reveal a shift of optical spectral weights towards higher energies, as temperature is lowered below the structural phase transition. This behavior may be understood from the structural modifications revealed from the new structure refinements of x-ray diffraction data from high quality single crystals. Apart from Ba atoms, some Ge cage atoms are also shifted into distant split sites below the phase transition. In this way one covalent bond is broken between the corresponding Ge atoms and they become threefold bonded. Electronic band structure calculations for the low symmetry ordered model show that the bond breaking causes a shifting of three bands from the conduction to the valence region. This leads to a shifting of optical spectral weights towards higher energies, which is in agreement with the experimental data.

#### IX-V-9 Indirect and Direct Energy Gaps in Kondo Semiconductor YbB<sub>12</sub>

OKAMURA, Hidekazu<sup>1</sup>; MICHIZAWA, Takahiro<sup>1</sup>; NANBA, Takao<sup>1</sup>; KIMURA, Shin-ichi; IGA, Fumitoshi<sup>2</sup>; TAKABATAKE, Toshiro<sup>2</sup> (<sup>1</sup>Kobe Univ.; <sup>2</sup>Hiroshima Univ.)

[*J. Phys. Soc. Jpn.* **74**, 1954–1957 (2005)]

The optical conductivity [ $\sigma(\omega)$ ] of the Kondo semiconductor YbB<sub>12</sub> has been measured over wide ranges of temperature ( $T = 8$ –690 K) and photon energy ( $h\nu \geq 1.3$  meV). The  $\sigma(\omega)$  data reveal the entire crossover of YbB<sub>12</sub> from a metallic electronic structure at high  $T$ 's to a semiconducting one at low  $T$ 's. Associated with the gap development in  $\sigma(\omega)$ , a clear onset is newly found at  $h\nu = 15$  meV for  $T \leq 20$  K. The onset energy is

identified as the gap magnitude of YbB<sub>12</sub> appearing in  $\sigma(\omega)$ . This gap in  $\sigma(\omega)$  is interpreted as the indirect gap, which has been predicted by the renormalized-band model of the Kondo semiconductor. On the other hand, the strong mid-infrared (mIR) peak observed in  $\sigma(\omega)$  is interpreted as arising from the direct gap. The absorption coefficient around the onset and the mIR peak indeed show the characteristic energy dependences expected for indirect and direct optical transitions in conventional semiconductors.

#### IX-V-10 Kondo Ground States and Non-Fermi-Liquid Behavior in CeNi<sub>1-x</sub>Co<sub>x</sub>Ge<sub>2</sub>

LEE, B. K.<sup>1</sup>; HONG, J. B.<sup>1</sup>; KIM, J. W.<sup>1</sup>; JANG, K.-H.<sup>1</sup>; MUN, E. D.<sup>1</sup>; JUNG, M. H.<sup>2</sup>; KIMURA, Shin-ichi; PARK, T.<sup>3</sup>; PARK, J. -G.<sup>1</sup>; KWON, Yong-seung<sup>1</sup> (<sup>1</sup>Sungkyunkwan Univ., Korea; <sup>2</sup>BKSI, Korea; <sup>3</sup>LANL, U.S.A.)

[*Phys. Rev. B* **71**, 214433 (9 pages) (2005)]

We report measurements of the magnetic susceptibility, specific heat, and electrical resistivity of the heavy fermion alloy series CeNi<sub>1-x</sub>Co<sub>x</sub>Ge<sub>2</sub>. With increasing  $x$ , hybridization between the localized 4f and conduction band electrons is enhanced. The magnetic order observed at  $x = 0$  is completely suppressed at  $x = 0.3$  and non-Fermi-liquid behavior appears at the critical concentration, which is analyzed in terms of two-dimensional antiferromagnetic quantum fluctuations. Specific heat and magnetic susceptibility data are quantitatively explained by the Coqblin-Schrieffer model with degenerate impurity spin  $j = 1/2, 3/2, \text{ and } 5/2$  for Co concentration range of  $x \leq 0.6, 0.7 \leq x \leq 0.8, \text{ and } x \geq 0.9$ , respectively.

#### IX-V-11 Infrared Spectroscopy under Multiextreme Conditions: Direct Observation of Pseudogap Formation and Collapse in CeSb

NISHI, Tatsuhiko<sup>1</sup>; KIMURA, Shin-ichi; TAKAHASHI, Toshiharu<sup>2</sup>; MORI, Yoshihisa<sup>3</sup>; KWON, Yong-seung<sup>4</sup>; IM, Hojun<sup>1</sup>; KITAZAWA, Hideaki<sup>5</sup> (<sup>1</sup>SOKENDAI; <sup>2</sup>Kyoto Univ.; <sup>3</sup>Okayama Univ. Sci.; <sup>4</sup>Sungkyunkwan Univ., Korea; <sup>5</sup>NIMS)

[*Phys. Rev. B* **71**, 220401(R) (4 pages) (2005)]

Infrared reflectivity measurements of CeSb under multiextreme conditions (low temperatures, high pressures, and high magnetic fields) were performed. A pseudogap structure, which originates from the magnetic band folding effect, responsible for the large enhancement in the electrical resistivity in the single-layered antiferromagnetic structure (AF-1 phase) was found at a pressure of 4 GPa and at temperatures of 35–50 K. The optical spectrum of the pseudogap changes to that of a metallic structure with increasing magnetic field strength and increasing temperature. This change is the result of the magnetic phase transition from the AF-1 phase to other phases as a function of the

magnetic field strength and temperature. This result is an important optical observation of the formation and collapse of a pseudogap under multiextreme conditions.

#### IX-V-12 Infrared Study on CeSb under High Pressures

**KIMURA, Shin-ichi; NISHI, Tatsuhiko<sup>1</sup>; MORI, Yoshihisa<sup>2</sup>; SUMIDA, Yukitsune<sup>2</sup>; TAKAHASHI, Toshiharu<sup>3</sup>; KWON, Yong-seung<sup>4</sup>; IM, Hojun<sup>1</sup>; KITAZAWA, Hideaki<sup>4</sup>**  
(<sup>1</sup>SOKENDAI; <sup>2</sup>Okayama Univ. Sci.; <sup>3</sup>Kyoto Univ.; <sup>4</sup>Sungkyunkwan Univ., Korea; <sup>5</sup>NIMS)

[*Physica B* **359-361**, 190–192 (2005)]

The optical reflectivity spectra ( $R(\omega)$ ) of CeSb have been measured at high pressures to investigate the origin of the physical properties appearing under pressures. At 300 K, the pressure dependence of  $R(\omega)$  revealed that the carrier density proportionally increases with increasing pressure up to 2.5 GPa. At lower temperature, the  $R(\omega)$  spectrum drastically changes with both temperature and pressure due to the complex magnetic phase diagram. Especially, at 2.5 GPa and 30 K, the  $R(\omega)$  intensity below 0.2 eV decreases, on the contrary that at around 0.3 eV increases. This result suggests that the density of states near the Fermi level decreases and shifts to the high-energy side.

#### IX-V-13 Electronic Structure of Bulk Metallic Glass $Zr_{55}Al_{10}Cu_{30}Ni_5$

**SODA, Kazuo<sup>1</sup>; SHIMBA, Kurando<sup>1</sup>; YAGI, Shinya<sup>1</sup>; KATO, Masahiko<sup>1</sup>; TAKEUCHI, Tsunehiro<sup>1</sup>; MIZUTANI, Uichiro<sup>1</sup>; ZHANG, T.<sup>2</sup>; HASEGARA, M.<sup>2</sup>; INOUE, Akihisa<sup>2</sup>; OTO, Takahiro; KIMURA, Shin-ichi**  
(<sup>1</sup>Nagoya Univ.; <sup>2</sup>Tohoku Univ.)

[*J. Electron Spectrosc. Relat. Phenom.* **144-147**, 585–587 (2005)]

The electronic structure of a bulk metallic glass  $Zr_{55}Al_{10}Cu_{30}Ni_5$  has been studied by means of photoelectron spectroscopy in order to understand the origins of its large glass formation ability and unique mechanical properties from the microscopic point of view. The valence-band photoelectron spectra show three bands ascribed to the Zr 4d, Ni 3d, and Cu 3d states. A remarkable feature of these bands is the highly symmetric spectral shape with the high-binding energy and narrow width in comparison with the d bands of the crystalline transition metals. This is attributed to the lack of the crystalline periodicity in the metallic glass as well as the reduction in the neighbouring atoms to hybridize with those transition metals. A high-resolution valence-band spectrum also reveals the intensity reduction near the Fermi level, which implies that the pseudo-gap in the electronic structure may be one of the important factors for the glass formation.

#### IX-V-14 Carrier-Induced Infrared Magnetic Circular Dichroism in the Magnetoresistive Pyrochlore $Tl_2Mn_2O_7$

**OKAMURA, Hidekazu<sup>1</sup>; KORETSUNE, Toshihisa<sup>1</sup>; KIMURA, Shin-ichi; NANBA, Takao<sup>1</sup>; IMAI, Hideto<sup>2</sup>; SHIMAKAWA, Yuichi<sup>2</sup>; KUBO, Yoshimi<sup>2</sup>**  
(<sup>1</sup>Kobe Univ.; <sup>2</sup>NEC Corp.)

[*J. Phys. Soc. Jpn.* **74**, 970–974 (2005)]

Infrared magnetic circular dichroism (MCD), or equivalently magneto-optical Kerr effect, has been measured on the  $Tl_2Mn_2O_7$  pyrochlore, which is well known for exhibiting a large magnetoresistance around the Curie temperature  $T_C \sim 120$  K. A circularly polarized, infrared synchrotron radiation is used as the light source. A pronounced MCD signal is observed exactly at the plasma edge of the reflectivity near and below  $T_C$ . However, contrary to the conventional behavior of MCD for ferromagnets, the observed MCD of  $Tl_2Mn_2O_7$  grows with the applied magnetic field, and not scaled with the internal magnetization. It is shown that these results can be basically understood in terms of a classical magnetoplasma resonance. The absence of a magnetization-scaled MCD indicates a weak spin-orbit coupling of the carriers in  $Tl_2Mn_2O_7$ . We discuss the present results in terms of the microscopic electronic structures of  $Tl_2Mn_2O_7$ .

#### IX-V-15 Magnetic Ordering in Frustrated $Ce_5Ni_2Si_3$

**LEE, B. K.<sup>1</sup>; RYU, D. H.<sup>1</sup>; KIM, D. Y.<sup>1</sup>; HONG, J. B.<sup>1</sup>; JUNG, M. H.<sup>2</sup>; KITAZAWA, Hideaki<sup>3</sup>; SUZUKI, Osamu<sup>3</sup>; KIMURA, Shin-ichi; KWON, Yong-seung<sup>1</sup>**  
(<sup>1</sup>Sungkyunkwan Univ., Korea; <sup>2</sup>BKSI, Korea; <sup>3</sup>NIMS)

[*Phys. Rev. B* **70**, 224409 (5 pages) (2004)]

The transport, magnetic, and thermal properties are studied on an antiferromagnetic compound  $Ce_5Ni_2Si_3$  with  $T_N = 7.3$  K. We find signatures of spin fluctuation in this geometrically frustrated magnet. The Curie-Weiss fit gives a large value of the paramagnetic Curie temperature, yielding a frustration parameter  $f = 8.4$ . The electronic specific heat coefficient  $\gamma = 300$  mJ/Ce mol  $K^2$  is strongly enhanced, leading to residual entropy at low temperatures. The spin fluctuation is suppressed as the magnetic field exceeds the metamagnetic transition field  $H_m = 1$  T, where the magnetoresistance decreases steeply. The steady increase of magnetic susceptibility below  $T_N$  is likely to be associated with the presence of paramagnetic Ce ions. For  $La_5Ni_2Si_3$ , a superconducting transition is observed at  $T_C = 1.8$  K.

#### IX-V-16 Features of Fluorescence Spectra of Polyethylene Terephthalate Films

**OUCHI, Isuke<sup>1</sup>; NAKAI, Ikuo<sup>2</sup>; ONO, Mitsumasa<sup>3</sup>; KIMURA, Shin-ichi**  
(<sup>1</sup>Tokushima Bunri Univ.; <sup>2</sup>Tottori Univ.; <sup>3</sup>Teijin DuPont Films Japan Ltd.)

[*Jpn. J. Appl. Phys.* **43**, 8107–8114 (2004)]

Out of two species of fluorescence of polyethylene terephthalate (PET), intrinsic fluorescence (I), which was caused by short-wavelength ( $< 320$  nm) excitation, was dominant for very thin films (less than a few microns), while, trap fluorescence (II), excited at longer wavelengths ( $> 320$  nm), was much more intense for thick films. This fact was confirmed, and explained by an elementary formula. Effects of polymerization catalysts onto the fluorescence spectra were found to be indirect; namely, peak positions of the fluorescence were not affected by catalyst systems, while fluorescence intensity was sensitive not only to catalyst systems but also to minute differences in local surroundings. Effects of catalyst systems on the weak absorption bands at 338 nm and 354 nm were examined. Integrated excitation spectra were resolved; therein, a hidden  $n \rightarrow \pi^*$  state was found. Most likely, this is related with the weak absorptions at 338 nm and 354 nm, which are the major origins of fluorescence (II).

#### **IX-V-17 Anomalous Magnetic Properties and Non-Fermi-Liquid Behavior in Single Crystals of the Kondo Lattice $\text{CeNiGe}_{2-x}\text{Si}_x$**

**KIM, D. Y.<sup>1</sup>; RYU, D. H.<sup>1</sup>; HONG, J. B.<sup>1</sup>; PARK, J.-G.<sup>1</sup>; KWON, Yong-seung<sup>1</sup>; JUNG, M. A.<sup>1</sup>; JUNG, M. H.<sup>2</sup>; TAKEDA, Naoya<sup>3</sup>; ISHIKAWA, Masakazu<sup>3</sup>; KIMURA, Shin-ichi**  
(<sup>1</sup>*Sungkyunkwan Univ., Korea*; <sup>2</sup>*KBSI, Korea*; <sup>3</sup>*Univ. Tokyo*)

[*J. Phys.: Condens. Matter* **16**, 8323–8334 (2004)]

We report on the magnetic susceptibility, specific heat and electrical resistivity of the heavy fermion compounds  $\text{CeNiGe}_{2-x}\text{Si}_x$  ( $0 \leq x \leq 1$ ). Compounds with  $x < 1$  show antiferromagnetic order, which with increasing  $x$  shifts toward lower temperature owing to increased exchange coupling between the localized 4f magnetic moments and conduction electrons. Eventually, the magnetic order almost becomes absent, for  $x = 1$ . An anomaly observed in the specific heat is well interpreted by the Kondo model for a degenerate impurity spin  $J = 1/2$  in the Coqblin–Schrieffer limit. A coherence peak indicative of the formation of a Kondo lattice is found in the electrical resistivity, whose features are consistent with the results for the specific heat. Interestingly, there is a significant deviation from Fermi-liquid behaviour at the critical concentration  $x = 1$ . This deviation is attributed to a quantum phase transition in a model with two-dimensional antiferromagnetic fluctuations.

#### **IX-V-18 Sub-Natural Linewidth Auger Electron Spectroscopy of the 2s Hole Decay in HCl**

**ITO, Kenji; HIKOSAKA, Yasumasa; KANEYASU, Tatsuo; SHIGEMASA, Eiji**

Auger-photoelectron coincidence spectroscopy, in which Auger electrons are measured in coincidence with the corresponding photoelectrons, can be a power-

ful tool to elucidate the decay dynamics of the core-hole states followed by the productions of doubly charged atomic and molecular ions. In our coincidence method, we measure threshold photoelectrons as photoelectrons to attain high detection efficiency. We have applied the coincidence method to the 2s hole decay in HCl. We tuned photon energy at the Cl 2s ionization threshold of HCl, and recorded the Auger electron spectrum in coincidence with the threshold photoelectrons. We have observed the Auger lines associated with the formations of  $\text{HCl}^{++}[(\text{Cl } 2p)^{-1}(\text{V})^{-1}]$  states via the  $L_1L_{2,3}V$  Coster-Kronig transitions, which are much faster than other Auger decay processes such as the LVV transitions. Ordinary Auger spectrum measured without any coincidences shows only broad structures due to the wide natural linewidth of the 2s hole states (1.8 eV FWHM). In contrast, several peaks appear on the coincidence spectrum we obtained, thanks to the sub-natural linewidth regime which is achieved by the coincidence observation using the high resolution spectrometers.

# Laser Research Center for Molecular Science

## IX-W Developments and Researches of New Laser Materials

Although development of lasers is remarkable, there are no lasers which lase in ultraviolet and far infrared regions. However, it is expected that these kinds of lasers break out a great revolution in not only the molecular science but also in the industrial world.

In this project we research characters of new materials for ultraviolet and far infrared lasers, and develop new lasers by using these laser materials.

### IX-W-1 Growth and Scintillation Properties of Yb Doped Aluminate, Vanadate and Silicate Single Crystals

**YOSHIKAWA, Akira<sup>1</sup>; OGINO, Hiraku<sup>1</sup>; SHIM, Jan Bo<sup>1</sup>; KOCHURIKIN, V. V.<sup>2</sup>; NIKL, M.<sup>3</sup>; SOLOVIEVA, N.<sup>3</sup>; ONO, Shingo; SARUKURA, Nobuhiko; KIKUCHI, M.<sup>4</sup>; FUKUDA, Tsuguo<sup>1</sup>**  
(<sup>1</sup>Tohoku Univ.; <sup>2</sup>GPI; <sup>3</sup>Inst. Phys. AS CR; <sup>4</sup>Tohoku Fukushi Univ.)

[*Opt. Mater.* **26**, 529 (2004)]

For the purpose of quick screening for charge transfer (CT) transitions of Yb<sub>3</sub> in various hosts, (Lu<sub>1-x</sub>Yb<sub>x</sub>)<sub>3</sub>Al<sub>5</sub>O<sub>12</sub> (Yb:LuAG) with  $x = 0.05, 0.15, 0.30$  and (Y<sub>1-x</sub>Yb<sub>x</sub>)AlO<sub>3</sub> (Yb:YAP) with  $x = 0.05, 0.10, 0.30$  were grown by the micro-pulling-down method. (Y,Yb)VO<sub>4</sub> with strong wetting was grown by edge defined film-fed growth method and materials, which require moderate temperature gradient, such as Ca<sub>8</sub>(La,Yb)<sub>2</sub>(PO<sub>4</sub>)<sub>6</sub>O<sub>2</sub> and (Gd,Yb)<sub>2</sub>SiO<sub>5</sub> were grown by Czochralski method. Strong dependence of the CT luminescence decay time and intensity on temperature was observed for Yb-doped LuAG and YAP. Super fast decay with 0.85 ns decay time was observed in Yb(30%) doped YAP at room temperature. Though the emission intensity is weak at room temperature, it exceeds several times that of PbWO<sub>4</sub>. In addition, CT luminescence of Yb:YAP occurs at longer wavelength than in BaF<sub>2</sub>, which enables the usage of glass-based photomultiplier for the detection. In addition, higher stopping power will be expected due to the higher density host compared with BaF<sub>2</sub>.

### IX-W-2 Onset Detection of Solid-State Phase Transition in Estrogen-Like Chemical via Terahertz Transmission Spectroscopy

**QUEMA, Alex; GOTO, Masahiro; SAKAI, Masahiro; JANAIRO, Gerardo<sup>1</sup>; OENZERFI, Riadh; TAKAHASHI, Hiroshi; ONO, Shingo; SARUKURA, Nobuhiko**  
(<sup>1</sup>De La Salle Univ.)

[*Appl. Phys. Lett.* **85**, 3914 (2004)]

Solid-state phase transition onset in an endocrine-disrupting estrogen-like chemical (1,4-naphthol) is detected using terahertz transmission spectroscopy. The appearance of two absorption peaks and the sudden

upsurge of terahertz-radiation power at 210 K indicate the onset of the solid-state phase transition. Differential scanning microscopy reveals a first-order phase transition at around 240 K while temperature-dependent x-ray diffraction analysis shows the occurrence of such phenomenon also at around 240 K. This demonstrates the sensitivity of the terahertz spectroscopic technique to phase transition since it provides a signal before such phenomenon actually occurs.

### IX-W-3 Design Principle of Wide-Gap Fluoride Hetero-Structures for Deep Ultraviolet Optical Devices

**OENZERFI, Riadh; ONO, Shingo; QUEMA, Alex; GOTO, Masahiro; SAKAI, Masahiro; SARUKURA, Nobuhiko; NISHIMATSU, Takeshi<sup>1</sup>; TERAKUBO, Noriaki<sup>1</sup>; MIZUSEKI, Hiroshi<sup>1</sup>; KAWAZOE, Yoshiyuki<sup>1</sup>; SATO, Hiroki<sup>1</sup>; YOSHIKAWA, Akira<sup>1</sup>; FUKUDA, Tsuguo<sup>1</sup>**  
(<sup>1</sup>Tohoku Univ.)

[*J. Appl. Phys.* **96**, 7655 (2004)]

The design of fluoride-based optical devices for deep ultraviolet applications is discussed. Variations in the band-gap energy and band structure with respect to composition are investigated for Li<sub>(1-x)</sub>K<sub>x</sub>Ba<sub>(1-y)</sub>Mg<sub>y</sub>F<sub>3</sub> perovskites. The band-gap energy, lattice constant, and band structure of perovskitelike fluorides are estimated based on *ab initio* calculations within the local-density approximation. The lattice-matched double hetero-structure with direct band-gap compounds (Li<sub>(1-x)</sub>K<sub>x</sub>Ba<sub>(1-y)</sub>Mg<sub>y</sub>F<sub>3</sub> on either LiBaF<sub>3</sub> or KMgF<sub>3</sub> substrates) is promising for fabrication.

### IX-W-4 Terahertz Time-Domain Spectroscopy of Amino Acids and Polypeptides

**YAMAMOTO, Koji<sup>1</sup>; TOMINAGA, Keisuke<sup>1</sup>; SASAKAWA, Hiroaki<sup>1</sup>; TAMURA, Atsuo<sup>1</sup>; MURAKAMI, Hidetoshi; OHTAKE, Hideyuki; SARUKURA, Nobuhiko**  
(<sup>1</sup>Kobe Univ.)

[*Biophys. J.* **L22** (2005)]

Frequency-dependent absorption coefficients and refractive indices of amino acids (glycine and L-alanine) and polypeptides (polyglycine and poly-L-alanine) in the wavenumber region from 7 to 55 cm<sup>-1</sup>

were measured by terahertz timedomain spectroscopy. A vibrational band was observed at  $45.5\text{ cm}^{-1}$  for polyglycine, which was assigned as an interchain mode. The reduced absorption cross sections of the amino acids and polypeptides show power-law behavior. The exponents are different between the monomers and polymers, and those of the two polypeptides suggest that the time dependences of the total dipole moments are similar in the timescale of subpico- to picoseconds.

## IX-X Development and Research of Advanced Tunable Solid State Lasers

Diode-pumped solid-state lasers can provide excellent spatial mode quality and narrow linewidths. The high spectral power brightness of these lasers has allowed high efficiency frequency extension by nonlinear frequency conversion. Moreover, the availability of new and improved nonlinear optical crystals makes these techniques more practical. Additionally, quasi phase matching (QPM) is a new technique instead of conventional birefringent phase matching for compensating phase velocity dispersion in frequency conversion. These kinds of advanced tunable solid-state light sources, so to speak "Chroma Chip Lasers," will assist the research of molecular science.

In this projects we are developing Chroma Chip Lasers based on diode-pumped-microchip-solid-state lasers and advanced nonlinear frequency conversion technique.

### IX-X-1 Spectroscopic Properties of Yb:GdVO<sub>4</sub> Single Crystal: Stark Levels, Selection Rules, and Polarized Cross Sections

SATO, Yoichi; TAIRA, Takunori; NAKAMURA, Osamu<sup>1</sup>; FURUKAWA, Yasunori<sup>1</sup>  
(<sup>1</sup>OXIDE)

[OSA Topical Meeting of Advanced Solid State Photonics MF8 (2005)]

Spectroscopic properties Yb:GdVO<sub>4</sub> single crystals were investigated. We determined the stark levels and discussed about the selection rules. We found that the 1030.7-nm transition from the lowest level in upper manifold to the highest level in lower manifold was forbidden transition in  $\pi$ -polarization. The absorption cross section, stimulated emission cross section, and radiative lifetime were also evaluated.  $\sigma_{ab}$  and  $\sigma_{em}$  at 948-nm were  $6.1$  and  $6.7 \times 10^{-20}$ -cm<sup>2</sup>, respectively. The calculated radiative lifetime of Yb:GdVO<sub>4</sub> was 313- $\mu$ s, and was consistent to the reported fluorescence lifetime of 320- $\mu$ s. From the wave-profiles of  $\sigma_{em}$  and polarized decay rate, the averaged wavelength of fluorescence was estimated to be 991-nm. If the pumping wavelength is set to 1000-nm, the absorption coefficient of 15 at.% Yb:GdVO<sub>4</sub> is still 9.8-cm<sup>-1</sup>, and laser cooling effect should be observed. Obtained spectroscopic parameters in this work were consistent with the previous report of laser oscillation. Authors also indicate that Yb:GdVO<sub>4</sub> has enough absorption at pumping wavelength for laser cooling.

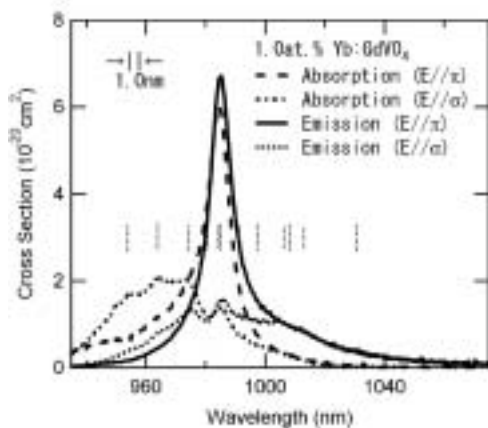


Figure 1. Polarized absorption and stimulated emission cross sections of Yb:GdVO<sub>4</sub>.

### IX-X-2 Spectroscopic Properties of All-Ceramic Composite with Layer-by-Layer of Nd:Y<sub>3</sub>Al<sub>5</sub>O<sub>12</sub> and Nd:Y<sub>3</sub>ScAl<sub>4</sub>O<sub>12</sub>

SATO, Yoichi; TAIRA, Takunori; IKESUE, Akio<sup>1</sup>  
(<sup>1</sup>JFCC)

[Conf. Lasers Electro-Optics JTuC28 (2005)]

The ceramic laser materials have been greatly interested because of their possibility for advanced lasers. The technique of composite ceramics has been especially considered to be the most important in the ceramics. Recently, this new ceramics technology about composite ceramics has been realized. In this work, we fabricated the all-ceramic composite with layer-by-layer of Nd:Y<sub>3</sub>ScAl<sub>4</sub>O<sub>12</sub> (YSAG) and Nd:Y<sub>3</sub>Al<sub>5</sub>O<sub>12</sub> (YAG).

The wide emission bandwidth of 5.5 nm in Nd:YSAG is composed of three transitions ( $R_1$ - $Y_1$ ,  $R_1$ - $Y_2$ ,  $R_2$ - $Y_3$ ), and contains the valley in its profile. The ratio of peak-to-valley is almost 50%, which reaches 93% in Nd:YAG. Fortunately, the valley in the emission band of Nd:YSAG overlaps the peak in the emission band of Nd:YAG. When we pumped from YSAG side with 809.0 nm pumping source, this peak-to-valley improved to 43%. If we fabricate the three-layered composite of YAG, YSAG, and Y<sub>3</sub>Sc<sub>2</sub>Al<sub>3</sub>O<sub>12</sub>, this specimen will perform more flat emission band. These profiles of fluorescence in Figure 1 are related to the effective emission cross-section, thus we can design the gain profile of this layered composite material. Even in the case of diode-pumping, we can control the spectroscopic properties by tuning the temperature of laser diode.

As a result, we found that the tuning of the pumping wavelength made the spectral profile of fluorescence from the composite ceramics more even than that from single-layered Nd:Y<sub>3</sub>Sc<sub>x</sub>Al<sub>5-x</sub>O<sub>12</sub> ceramics. The technique of composite ceramics is proved to be useful because it can provide not only the compositional tuning but also a new controllability by the selection of the pump source.

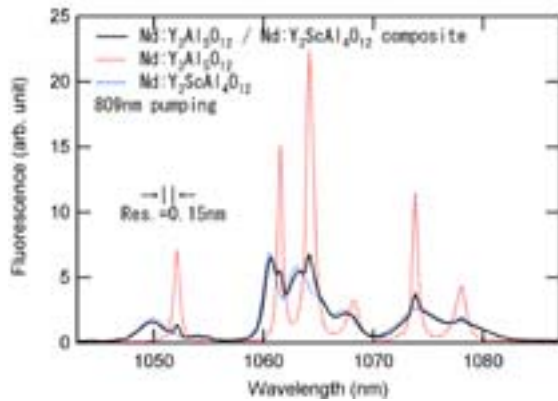


**Figure 1.** Fluorescence profiles of 1.0at.% Nd:YAG, Nd:YSAG, and their composite.

### IX-X-3 Hybrid Process for Measurement of Spectroscopic Properties of Nd:GdVO<sub>4</sub>

SATO, Yoichi; TAIRA, Takunori

[*Pac. Rim Conf. Lasers Electro-Optics CWI2-5* (2005)]

In order to construct highly performing solid-state lasers, laser materials should be able to absorb efficiently the pump radiation. The request of high pump absorption efficiency is more important for the case in microchip laser scheme, or under direct pumping into the emitting levels. Rare-earth doped vanadate crystals are the promised candidates solid-state lasers with high-performance because of their desirable properties of high optical absorption. However, there are many reports for an absorption cross section of the transition between  $^4I_{9/2}$  and  $^4F_{5/2}$  in Nd:GdVO<sub>4</sub>. In this paper, authors discussed how to evaluate the spectroscopic properties of Nd- and Yb-doped GdVO<sub>4</sub> crystals.

We propose the “Hybrid Process” which is shown in Figure 1 as a technique for the spectroscopic evaluation in order to avoid overlooking the influences of emission in absorption and the influences of absorption in emission by simultaneous evaluation. This process also gives the radiative quantum efficiency ( $\eta_r$ ). We studied Nd:GdVO<sub>4</sub> (Shandong Newphotonics) and Nd:YVO<sub>4</sub> (ITI) according to the Hybrid Process.

As a result, rare-earth doped vanadate crystals are the promised candidates solid-state lasers due to their large cross sections and relatively high thermal conductivity. In order to perform these superior characteristics, we have to notice that heavy heat generation under non-lasing condition and the difference in the thermal conductivity depending on the crystal-axis.

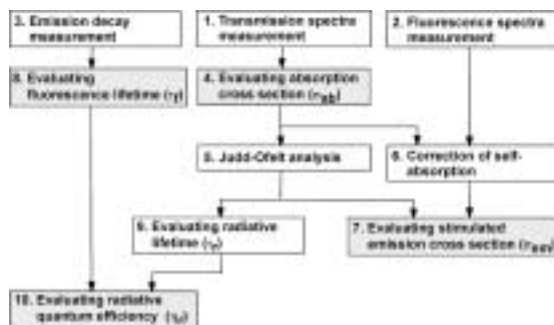


**Figure 1.** The flow-chart of “Hybrid Process” for measurement of the spectroscopic properties in Nd:vanadate.

### IV-X-4 Absorption, Emission Spectrum Properties and Efficient Laser Performances of Yb:Y<sub>3</sub>ScAl<sub>4</sub>O<sub>12</sub> Ceramics

SAIKAWA, Jiro; SATO, Yoichi; TAIRA, Takunori; IKESUE, Akio<sup>1</sup>  
(<sup>1</sup>JFCC)

[*Appl. Phys. Lett.* **85**, 1898 (2004)]

We report on the continuous-wave laser performances of Yb<sup>3+</sup>-doped disordered Y<sub>3</sub>Al<sub>5</sub>O<sub>12</sub>/Y<sub>3</sub>Sc<sub>2</sub>Al<sub>4</sub>O<sub>12</sub> (YAG/YSAG) ceramics fabricated by sintering method. These new materials exhibit relatively low minimum pump intensity ( $I_{\min}$ ) and broad emission bandwidth even in the yttrium aluminum garnet systems. The value of  $I_{\min}$  in the Yb:Y<sub>3</sub>ScAl<sub>4</sub>O<sub>12</sub> ceramics was found to be 2/3 compared with the Yb:YAG single crystal under 970-nm zero-line pumping. Efficient laser oscillation of 72% slope efficiency was obtained for input pump power. These materials attract great interest for high power femtosecond microchip lasers and amplifier applications.

### IX-X-5 Passive Mode Locking of a Mixed Garnet Yb:Y<sub>3</sub>ScAl<sub>4</sub>O<sub>12</sub> Ceramic Laser

SAIKAWA, Jiro; SATO, Yoichi; TAIRA, Takunori; IKESUE, Akio<sup>1</sup>  
(<sup>1</sup>JFCC)

[*Appl. Phys. Lett.* **85**, 5845 (2004)]

We have demonstrated a passively mode-locked Yb<sup>3+</sup>-doped Y<sub>3</sub>ScAl<sub>4</sub>O<sub>12</sub> ceramic laser, which is a solid solution of Y<sub>3</sub>Al<sub>5</sub>O<sub>12</sub> (YAG) and Y<sub>3</sub>Sc<sub>2</sub>Al<sub>4</sub>O<sub>12</sub> (YSAG), by using a semiconductor saturable-absorber mirror (SESAM). The maximum average output power was as high as 150 mW with a pulse duration of 500 fs. With a 0.5% output coupler, pulses as short as 280 fs having an average output power of 62 mW at 1035.8 nm were obtained.

### IX-X-6 High-Power Operation of Diode Edge-Pumped, Glue-Bonded, Composite Yb:Y<sub>3</sub>Al<sub>5</sub>O<sub>12</sub> Microchip Laser with Ceramic, Undoped YAG Pump Light-Guide

TSUNEKANE, Masaki; TAIRA, Takunori

[*Jpn. J. Appl. Phys.* in press]

The high-power operation of a diode edge-pumped, composite Yb<sup>3+</sup>-doped Y<sub>3</sub>Al<sub>5</sub>O<sub>12</sub> (Yb:YAG) microchip laser has been demonstrated. The novel composite microchip has a 5-mm-diameter, 300- $\mu$ m-thickness, single-crystal Yb:YAG core and a transparent ceramic, undoped YAG pump light-guide surrounding the core with the same thickness. The high-reflection coated face of the microchip was bonded to a water-cooled heat-sink by a thermally conductive glue for efficient con-

ductive cooling. The pump light from a fourfold diode stack directly coupled to the light-guide and maximum output powers of 410 W (peak) and 285 W have been successfully obtained at an input pump power of 866 W in quasi-continuous-wave (10 ms, 10 Hz) and continuous-wave operations, respectively, at room temperature.

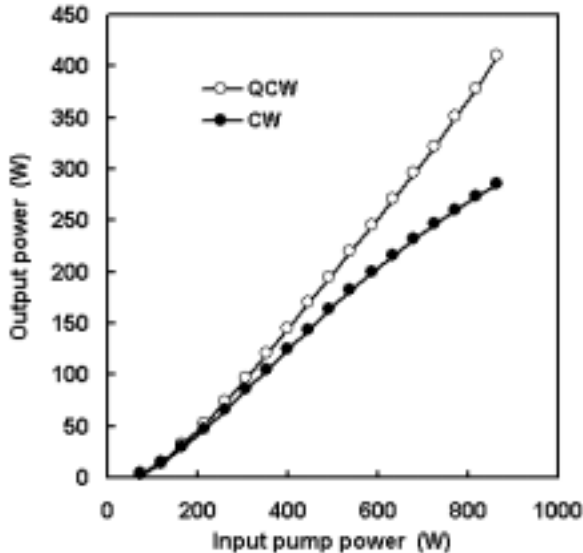


**Figure 1.** Input pump power versus laser output power of diode edge-pumped, composite Yb:YAG microchip laser in QCW and CW operations at room temperature.

#### IX-X-7 Continuous-Wave Deep Blue Generation in a Periodically Poled MgO:LiNbO<sub>3</sub> Crystal by Single-Pass Frequency Doubling of a 912-nm Nd:GdVO<sub>4</sub> Laser

MIZUUCHI, Kiminori<sup>1</sup>; MORIKAWA, Akihiro<sup>1</sup>; SUGITA, Tomoya<sup>1</sup>; YAMAMOTO, Kazuhisa<sup>1</sup>; PAVEL, Nicolaie<sup>2</sup>; TAIRA, Takunori  
(<sup>1</sup>Matsushita Co., Ltd.; <sup>2</sup>IAP-NILPRP, Romania)

[*Jpn. J. Appl. Phys.* **43**, L1293 (2004)]

We report blue emission at 456 nm by single-pass second-harmonic generation in a bulk periodically-poled MgO:LiNbO<sub>3</sub> crystal, for the first time to our best knowledge. Using as a pumping source a continuous-wave Nd:GdVO<sub>4</sub> laser operating at 912 nm, blue power of 167 mW with 8.3% infrared-to-blue conversion efficiency and 4.2%/W normalized conversion efficiency was obtained. The present data, combined with our previous results on green generation, supports the prospect of obtaining compact and high power visible sources based on bulk periodically poled MgO:LiNbO<sub>3</sub>.

#### IX-X-8 Continuous-Wave Ultraviolet Generation at 354-nm in a Periodically Poled MgO:LiNbO<sub>3</sub> by Frequency Tripling of a Diode End-Pumped Nd:GdVO<sub>4</sub> Microlaser

MIZUUCHI, Kiminori<sup>1</sup>; MORIKAWA, Akihiro<sup>1</sup>; SUGITA, Tomoya<sup>1</sup>; YAMAMOTO, Kazuhisa<sup>1</sup>; PAVEL, Nicolaie<sup>2</sup>; TAIRA, Takunori  
(<sup>1</sup>Matsushita Co., Ltd.; <sup>2</sup>IAP-NILPRP, Romania)

[*Appl. Phys. Lett.* **85**, 3959 (2004)]

Irregular side spread of polarization inversion was suppressed in PPMgLN up to 2-mm thickness by using a multipulse poling method. Cascaded THG was performed by employing a first-order SHG-QPM PPMgLN followed by a SFG-QPM PPMgLN stage, and a 1063 nm Nd:GdVO<sub>4</sub> laser as a pumping source. CW power of 47 mW at 354 nm with 3.9%/W/cm normalized conversion efficiency was obtained. To our knowledge this is the first demonstration in PPMgLN of such a system and the highest UV power at 354 nm reported by CW single-pass process in a QPM structure. The present result supports the prospect of obtaining compact and high power UV source based on bulk periodically poled MgO:LiNbO<sub>3</sub>.

#### IX-X-9 High-Power Continuous-Wave Intracavity Frequency-Doubled Nd:GdVO<sub>4</sub>-LBO Laser under Diode Pumping into the Emitting Level

PAVEL, Nicolaie<sup>1</sup>; TAIRA, Takunori  
(<sup>1</sup>IAP-NILPRP, Romania)

[*IEEE J. Sel. Top. Quantum Electron.* **11**, 631 (2005)]

Continuous-wave emission in Nd:GdVO<sub>4</sub> at the 1- $\mu$ m fundamental wavelength and 531-nm second harmonic, which was obtained by intracavity frequency-doubling with LBO, is investigated under end-pumping with high-power diode laser at 808 and 879 nm. The maximum green power of 5.1 W with 0.31 overall optical-to-optical efficiency in a beam of  $M^2 = 1.46$  was obtained under 879-nm pumping, directly into the <sup>4</sup>F<sub>3/2</sub> emitting level. To the authors best knowledge this is the highest CW green power obtained for the Nd:GdVO<sub>4</sub> laser material.

#### IX-X-10 Deep Blue Generation at 456 nm in a Periodically Poled MgO:LiNbO<sub>3</sub> Ridge-Type Waveguide by Single-Pass Frequency Doubling of a Nd:GdVO<sub>4</sub> Micro-Laser

PAVEL, Nicolaie<sup>1</sup>; TAIRA, Takunori; IWAI, Makato<sup>2</sup>; YOSHINO, Takeshi<sup>2</sup>; IMAEDA, Minoru<sup>2</sup>  
(<sup>1</sup>IAP-NILPRP, Romania; <sup>2</sup>NGK)

[*Conf. Lasers Electro-Optics CTuC30* (2005)]

This paper reports on our work toward scaling deep blue light by SHG-QPM process in a PPMgLN ridge-type waveguide: 93 mW power at 456 nm was achieved by single-pass SHG of a 912-nm Nd:GdVO<sub>4</sub> laser.

#### IX-X-11 Efficient 1.06 and 1.34- $\mu$ m Laser Emission of Highly-Doped Nd:YAG under 885-nm Diode Pumping into the Emitting Level

PAVEL, Nicolaie<sup>1</sup>; TAIRA, Takunori  
(<sup>1</sup>IAP-NILPRP, Romania)

[*European Conf. Lasers Electro-Optics CA-19-MON* (2005)]

This work reports on 1.34- $\mu\text{m}$  emission in Nd:YAG under direct pumping into the emitting level, at 885 nm, the first demonstration of such a system to the best of our knowledge. CW output power of 3.8 W at 1.34  $\mu\text{m}$  with overall optical-to-optical efficiency of 0.26 is obtained from a 2.5-at.% Nd:YAG single crystal pumped into the  $^4F_{3/2}$  level with a high-brightness 885-nm diode laser. The influence of the lasing wavelength and medium concentration on the thermal effects induced by optical pumping into the active component is discussed. It is shown that laser emission at 1.3  $\mu\text{m}$  increases the thermal effects in medium only under a certain value of  $C_{Nd}$ . This behavior was checked by mapping the temperature of the output surface of the Nd:YAG crystals. These results demonstrate that diode laser pumping into the emitting level of concentrated Nd-based laser materials is a solution for construction of efficient micro-lasers and for scaling to high power.

#### **IX-X-12 High-Power Multi-Pass Pumped Microchip Nd:GdVO<sub>4</sub> Laser**

**PAVEL, Nicolaie<sup>1</sup>; TAIRA, Takunori**  
(<sup>1</sup>IAP-NILPRP, Romania)

[*Pacific Rim Conf. Lasers Electro-Optics* CTuI3-5  
(2005)]

We describe a continuous-wave thin-disk Nd:GdVO<sub>4</sub> laser in a multi-pass pumping scheme. Employing a 250- $\mu\text{m}$  thick, 0.5-at.% Nd:GdVO<sub>4</sub> crystal, a maximum output power of 13.9 W was obtained for 22 W absorbed power; the slope efficiency in absorbed power was 0.65. Pumping at 879 nm, directly into the  $^4F_{3/2}$  emitting level, resulted in laser operation with slope efficiency in absorbed power of 0.69; the laser output power was 3.6 W at an absorbed pump power of 6.2 W. We appreciate that with an improved heat transfer between the Nd:GdVO<sub>4</sub> and the cooling system, a Nd:GdVO<sub>4</sub> medium of lower doping and an increased number of passes of the pump radiation, this geometry could be also a good solution for efficient laser emission at 912 nm.

#### **IX-X-13 Highly Efficient New Pumping Configuration for Microchip Solid State Laser**

**DASCALU, Traian<sup>1</sup>; TAIRA, Takunori**  
(<sup>1</sup>IAP-NILPRP, Romania)

[*European Conf. Lasers Electro-Optics* CThu4-2  
(2005)]

We propose a new pumping scheme which allows 94% absorption efficiency in Yb:YAG 15 at.% with 200  $\mu\text{m}$  thickness with uniform pump distribution. This configuration can be scaled up and it is very attractive especially for high power quasi-4-levels lasers where the reabsorption losses are important.

#### **IX-X-14 High Energy Quasi-Phase-Matched Optical Parametric Oscillation in a 3-mm-Thick Periodically Poled MgO:LiNbO<sub>3</sub> Device**

**ISHIZUKI, Hideki; SHOJI, Ichiro; TAIRA, Takunori**

[*Opt. Lett.* **29**, 2527 (2004)]

We presented high energy optical parametric oscillation (OPO) using 3-mm-thick periodically poled MgO:LN (PPMgLN) device. The maximum total output energy of 22 mJ at the pump energy of 46 mJ was obtained using a Q-switched Nd:YAG laser of 30 Hz repetition rate with 15 ns pulse duration. The large-aperture PPMgLN devices would enable us to realize high-energy wavelength conversion, short pulse amplification, and pulse compression.

# Equipment Development Center

## IX-Y Development of New Instruments and Experimental Devices

The technical staff of the Equipment Development Center is partly engaged in planning, researching, designing and constructing high technology experimental instruments in collaboration with the scientific staff. And these experimental instruments are incorporated with new manufacturing technology and new mechanical idea.

### IX-Y-1 Development of a High-Precision Slit Blade for the Transmission-Grating Spectrometer

**KONDO, Takuhiko; SUZUI, Mitsukazu; TORII, Tatsuharu<sup>1</sup>; MASUDA, Tadashi<sup>1</sup>; HORIGOME, Toshio; HATSUI, Takaki**  
 (<sup>1</sup>Nagoya Univ.)

Development of the transmission-grating spectrometer for soft X-ray emission spectroscopy has been carried out by the Department Vacuum UV PhotoScience.

In order to improve further the energy resolution of the spectrometer, an entrance slit with the minimum slit opening of 1mm has been developed. In order to maintain the spectrometer efficiency, the distance between the sample and the slit is designed to be less than 1 mm. Accordingly, the slit blades are to be smaller than  $13 \times 10 \times 2.5 \text{ mm}^3$ . These requirements demanded a development of slit blades with a roughness of less than  $0.3 \mu\text{m}$  using a high-precision polishing process.

The blades were polished first on the side A and B (Figure 1). The resulting roughness was less than  $R_a 7 \text{ nm}$ . The edge surfaces were polished by using a clamp as shown in Figure 2. The four blades were pressed by the two plates via two screws (M4) so as to minimize the gap between the blades. The pressure was optimized so that the pile up did not occur during the polishing process. The resulting slit blade is shown in Figure 3. Figure 4 is the top view of the slit blade from A side. The edge roughness was about  $0.3 \mu\text{m}$ .

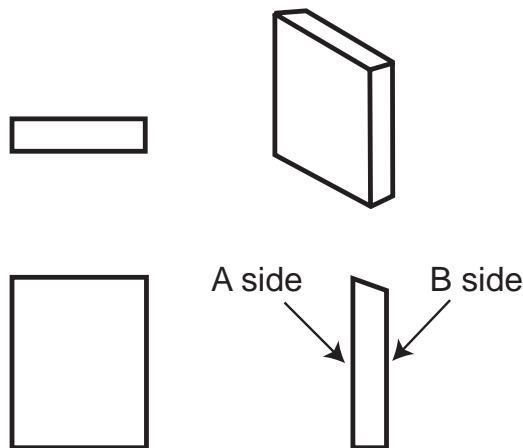


Figure 1. Schematic view of the slit blade.

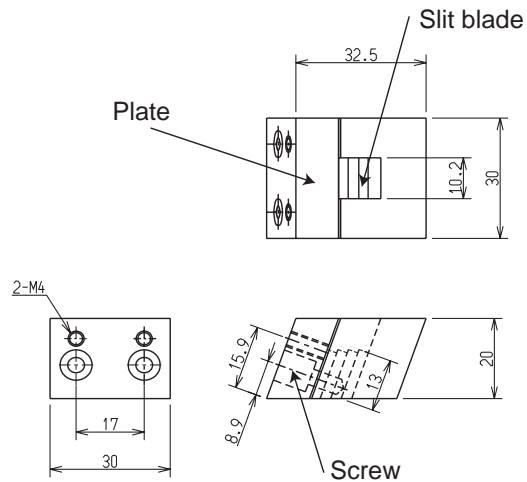


Figure 2. The clamp for the polishing of the edge surfaces.



Figure 3. Photograph of the slit.

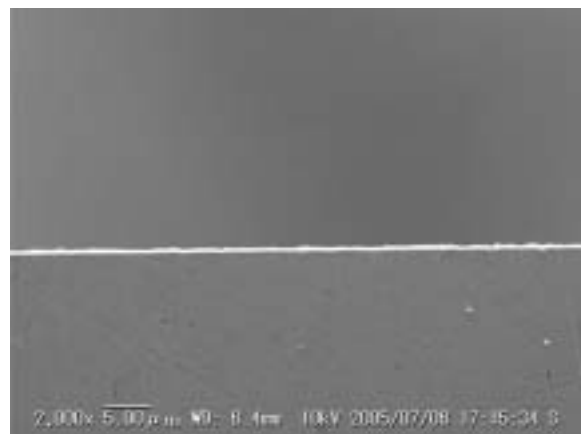


Figure 4. Top view of the slit blade observed by SEM.

## IX-Y-2 Manufacture of Glass Microreactor Chips

AOYAMA, Masaki; SUZUI, Mitsukazu;  
FUKUYAMA, Naoshi; YAMADA, Yoichi M. A.;  
UOZUMI, Yasuhiro

Glass microreactor chips used for catalyst research in Research Center for Molecular-scale Nanoscience were manufactured.

Although glass chips are usually manufactured by photolithography and wet etching, it takes expense and time to manufacture many arbitrary flow patterns. Then, we attached the diamond grinding tool in the general machine tool, and processed flow patterns into it.

The SEM photograph of flow patterns of a chip is shown in Figure 1. The quality of the material was PYREX glass, and the slot width and depth were 100  $\mu\text{m}$  and 40  $\mu\text{m}$ , respectively. Although generating of the deficit of a detailed crack and edge could become a problem in processing of a brittle material, it was processed by spindle speed 50,000 rpm, feed rate 1.0 mm/min, the depth of cut 5  $\mu\text{m}$ , and diamond tool particle size #1000, and good flow patterns whose processing side coarseness were about 1.5  $\mu\text{m}$  were obtained.

Such processing technology is applied to processing of brittle material such as silicone in addition to glass, and is useful also to manufacture of the micro parts for Department of Vacuum UV Photoscience.

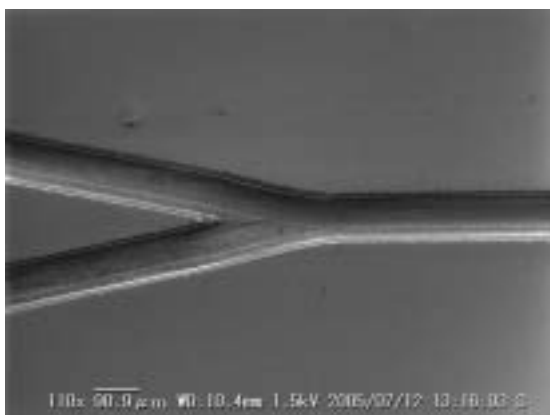


Figure 1. Flow patterns of a chip.

## IX-Y-3 Micro Processing by a Femto-Second Laser

AOYAMA, Masaki; YANO, Takayuki; SUZUI, Mitsukazu; SASAKI, Ryuichiro<sup>1</sup>; NAGAI, Hiroyuki<sup>1</sup>; YOSHIDA, Makoto<sup>1</sup>; TAKAHASHI, Kazuyuki; KOBAYASHI, Hayao; RAHMAN, Md. Mashiur; URISU, Tsuneo  
(<sup>1</sup>AISHIN Seiki Co., Ltd.)

Micro fabrication processing was done by using the femto-second fiber laser (FCP $\mu$ Jewel B-250) manufactured by IMRA in laboratory of AISHIN Seiki Co., Ltd.

Processing conditions are center wavelength 1560 nm, pulse width 900 fs, and repetition frequency 256

kHz. The main two cases are described in the following.

Diamond Anvil Cell for the high pressure experiment will be used by Department of Molecular Assemblies. In order to draw four probes out of the sample cavity of Diamond Anvil Cell, the groove for the wiring on the metal gasket of Diamond Anvil Cell is necessary. Schematic view of the metal gasket for the high pressure experiment is shown in Figure 1. The hole is at the center of gasket plate (8  $\times$  8  $\times$  0.3 mm<sup>3</sup> Inconel 625) and a diameter of 0.4 mm. Prepressing between both sides of the plate by Diamond Anvil resulted in the basin-like plastic deformation of the whole plate and a height of about 20  $\mu\text{m}$  of the swelling around the central hole. In order to pass through the wiring with a diameter of 10  $\mu\text{m}$ , the required groove width and depth are considered to be about 50  $\mu\text{m}$  and 30  $\mu\text{m}$ , respectively.

Excellent groove processing was attained in a short term with no heat effect on the sharpness of the edge and no deposition by melting. This result is shown in Figure 2.

It was applied to hole processing for the biosensor device used in Department of Vacuum UV Photoscience. An AFM measurement after hole processing is shown in Figure 3. Drilling of the Cobalt layer on SiO<sub>2</sub> with a diameter of about 1.5  $\mu\text{m}$  could be achieved by adjusting laser power and an exposure time.

A trial of the partial removal of a gold thin film from a circuit pattern on the SiO<sub>2</sub>-covered silicon substrate by the femto-second laser is now in progress.

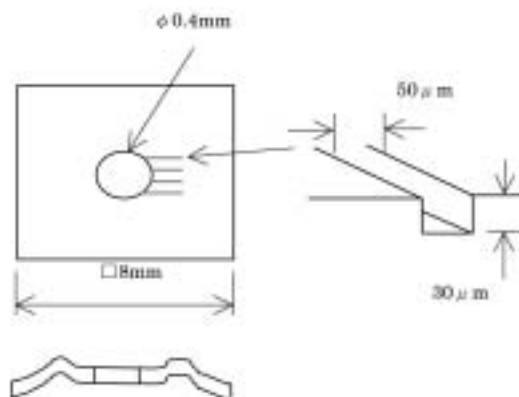


Figure 1. Schematic view of the metal gasket.

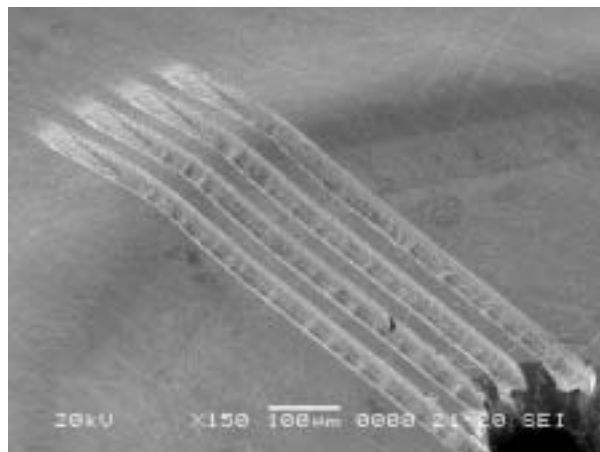


Figure 2.

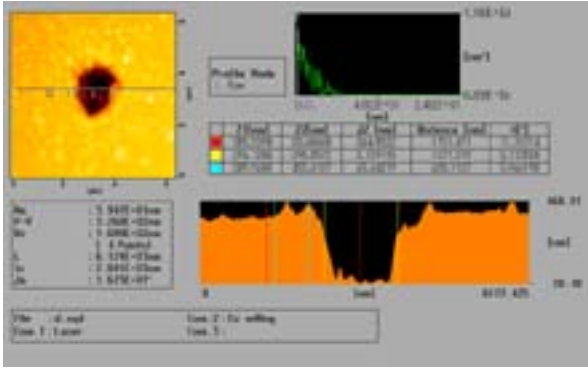


Figure 3. The measurement result of the cross section profile of a hole.

**IX-Y-4 Development of Electrical Control System of Fluorescence Recovery after Photobleaching Apparatus Using Semiconductor Laser for Illumination**

YOSHIDA, Hisashi; URISU, Tsuneo

We have developed the electrical control system of the fluorescence recovery after photobleaching (FRAP) apparatus as schematically shown in Figure 1. Two recording devices are equipped in the setup. One is a charge coupled device (CCD) by which the sample surface image and the photobleached spot image are monitored. The other one is photo-multiplier (PMT) by which the time dependence of the fluorescence intensity at the photobleaching spot can be monitored. A pinhole with 100 μm diameter is set at the confocal point of the microscope before the PMT. Two neutral density filters with different transmission coefficients are inserted to the filter holder to attenuate the UV lamp and laser intensities, respectively. The UV lamp illumination was used mainly for sample setting and was turned off during the photobleaching and the fluorescence recovery process. The photo-multiplier recording, which gives the time dependence of the fluorescence recovery directly, is very convenient in the calculation of the diffusion constant. The block diagram of a laser driving and the photo-multiplier detection system is shown in Figure 2. The semiconductor laser is drove by the bleaching pulse and succeeding pulse train of the sampling pulse.

The drive voltage 1.25 V correspond to the second harmonic output of ~5 mW. The fluorescence recovery can be monitored by the weak sampling pulse train without giving damage to dye molecules. The relation between the laser driving pulses and the photo-multiplier output monitoring pulse are shown also in Figure 2.

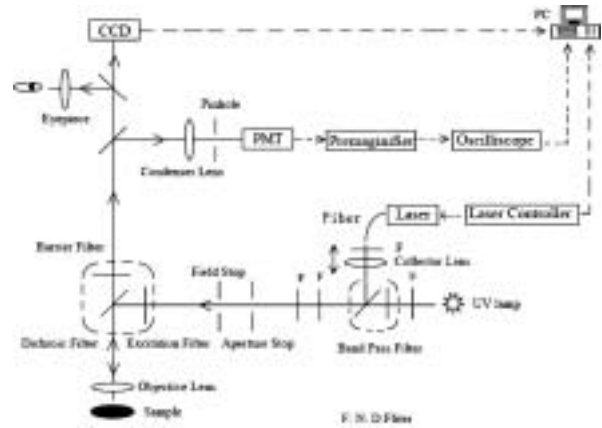


Figure 1.

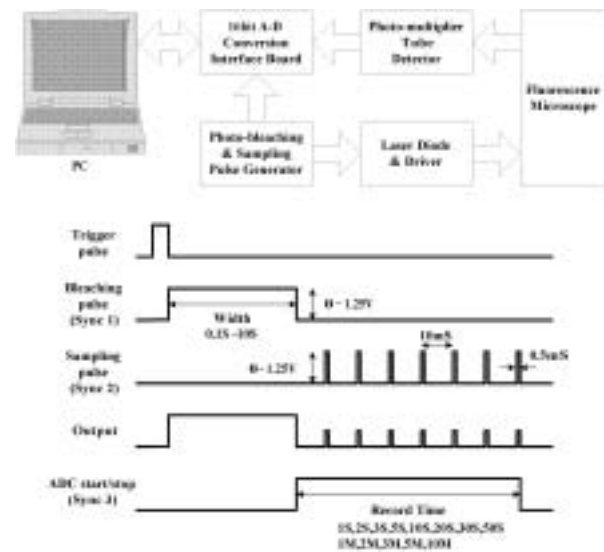


Figure 2.

## Safety Office

### IX-Z Development of Novel Heterocyclic Compounds and Their Molecular Assemblies for Advanced Materials

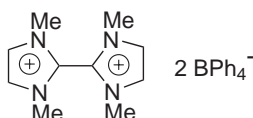
Heterocycles containing sulfur and/or nitrogen atoms are useful as components of functional materials since heteroatoms in their rings are helpful to stabilize ions or ion-radical species, and extended  $\pi$ -conjugation decreases Coulombic repulsion. In addition intermolecular interactions caused by heteroatom contacts can be expected to form novel molecular assemblies. In this project new electron acceptors, donors, and donor-acceptor compounds based on heterocycles such as 1,2,5-thiadiazole and 1,3-dithiole were synthesized and their properties including those of the charge-transfer complexes or ion-radical salts were investigated. Unique crystal structures were constructed by using weak intermolecular interactions such as hydrogen bonding or heteroatom contacts.

#### IX-Z-1 Molecular Arrangement in the Crystals of 1,1',3,3'-Tetramethyl-2,2'-bi-1*H*-imidazolium Bis(tetraphenylborate) with Ketone, Aldehyde, and Nitrile as Guest Molecules

ONO, Katsuhiko<sup>1</sup>; IWAO, Takeshi<sup>1</sup>; UCHIUMI, Hideki<sup>1</sup>; SUZUKI, Takahisa<sup>1</sup>; TOMURA, Masaaki<sup>1</sup>; OHKITA, Masakazu<sup>1</sup>; SAITO, Katsuhiko<sup>1</sup>  
(<sup>1</sup>Nagoya Inst. Tech.)

[*Bull. Chem. Soc. Jpn.* **78**, 867–872 (2005)]

1,1',3,3'-Tetramethyl-2,2'-bi-1*H*-imidazolium bis(tetraphenylborate), an ion-association compound, afforded inclusion crystals with a variety of guest molecules, such as ketone, aldehyde, and nitrile. X-ray crystallographic analyses revealed intermolecular interactions between the biimidazolium dication and the guest molecules in the inclusion crystals. Their contact modes depended on the molecular structures of the guest molecules, resulting in various molecular arrangements.



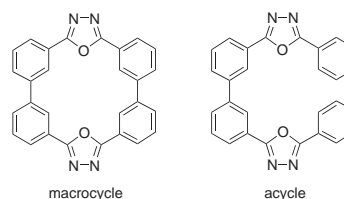
#### IX-Z-2 Macrocyclic and Acyclic Bis(2,5-diphenyl-1,3,4-oxadiazole)s with Electron-Transporting and Hole-Blocking Ability in Organic Electroluminescent Devices

ONO, Katsuhiko<sup>1</sup>; EZAKA, Seiichi<sup>1</sup>; HIGASHIBATA, Akinori<sup>1</sup>; HOSOKAWA, Ryohei<sup>1</sup>; OHKITA, Masakazu<sup>1</sup>; SAITO, Katsuhiko<sup>1</sup>; SUTO, Michitaka<sup>2</sup>; TOMURA, Masaaki<sup>1</sup>; MATSUSHITA, Yosuke<sup>3</sup>; NAKA, Shigeki<sup>3</sup>; OKADA, Hiroyuki<sup>3</sup>; ONNAGAWA, Hiroyoshi<sup>3</sup>  
(<sup>1</sup>Nagoya Inst. Tech.; <sup>2</sup>Dow Corning Asia Ltd.; <sup>3</sup>Toyama Univ.)

[*Macromol. Chem. Phys.* **206**, 1576–1582 (2005)]

Two types of bis(2,5-diphenyl-1,3,4-oxadiazole)s, macrocyclic and acyclic, were prepared and evaluated as electron-transporting and hole-blocking materials in

phosphorescent EL devices. Maximum efficiencies of  $\eta_{\text{ext}} = 10.4\%$  at  $J = 0.11 \text{ mA}\cdot\text{cm}^{-2}$  for the macrocycle and  $\eta_{\text{ext}} = 14.1\%$  at  $J = 3.01 \text{ mA}\cdot\text{cm}^{-2}$  for the acycle were observed. X-ray crystallographic analysis and DSC measurements revealed a strong intermolecular interaction between the macrocycles and weaker intermolecular interactions between the acycles. The EL characteristics depend on the intermolecular interactions.



#### IX-Z-3 Synthesis, Characterization and FET Properties of Novel Dithiazolylbenzothiadiazole Derivatives

AKHTARUZZAMAN, Md.<sup>1</sup>; KAMATA, Naoto<sup>1</sup>; NISHIDA, Jun-ichi<sup>1</sup>; ANDO, Shinji<sup>1</sup>; TADA, Hirokazu<sup>2</sup>; TOMURA, Masaaki<sup>1</sup>; YAMASHITA, Yoshiro<sup>3</sup>  
(<sup>1</sup>Tokyo Inst. Tech.; <sup>2</sup>IMS and Osaka Univ.; <sup>3</sup>IMS and Tokyo Inst. Tech.)

[*Chem. Commun.* 3183–3185 (2005)]

Novel dithiazolylbenzothiadiazole derivatives easily obtained show efficient fluorescence with high electron affinity. The FET device of a trifluoromethylphenyl derivative exhibited a good n-type performance with high electron mobility. Since substituents can be easily introduced to the  $\alpha$ -position of thiazole, the dithiazolylbenzothiadiazole unit would be useful as a core for unique electron-accepting  $\pi$ -conjugated molecules.

